PHOTONICS INSIGHTS

Topological photonics in metamaterials

Shaojie Ma,[a] Biao Yang,[b] and Shuang Zhang[a,c,*]
[a]Department of Physics, University of Hong Kong, Hong Kong, China
[b]College of Advanced Interdisciplinary Studies, National University of Defense Technology, Changsha, China
[c]Department of Electrical & Electronic Engineering, University of Hong Kong, Hong Kong, China

Abstract. Originally a pure mathematical concept, topology has been vigorously developed in various physical systems in recent years, and underlies many interesting phenomena such as the quantum Hall effect and quantum spin Hall effect. Its widespread influence in physics led the award of the 2016 Nobel Prize in Physics to this field. Topological photonics further expands the research field of topology to classical wave systems and holds promise for novel devices and applications, e.g., topological quantum computation and topological lasers. Here, we review recent developments in topological photonics but focus mainly on their realizations based on metamaterials. Through artificially designed resonant units, metamaterials provide vast degrees of freedom for realizing various topological states, e.g., the Weyl point, nodal line, Dirac point, topological insulator, and even the Yang monopole and Weyl surface in higher-dimensional synthetic spaces, wherein each specific topological nontrivial state endows novel metamaterial responses that originate from the feature of some high-energy physics.

Keywords: topological photonics; metamaterial; constitutive relation; semimetal.

Received Feb. 16, 2022; revised manuscript received May 6, 2022; accepted May 19, 2022; published online Aug. 18, 2022.

[DOI: 10.3788/PI.2022.R02]

1 Introduction

In geometry, topology[1] concerns the global features of a shape, independent of the detail—a famous example being that a coffee mug and a torus are topologically equivalent because they can be smoothly transformed into each other without experiencing dramatic changes, e.g., opening holes, tearing, gluing. The Euler characteristic χ is introduced to describe such a global invariant, which is defined by the integral of the Gaussian curvature $\vec{K}$ over a closed surface, $\chi = \frac{1}{2\pi}\int_S \vec{K}\cdot d\vec{A} \in \mathbb{Z}$, which is always an integer. Hence, it cannot vary continuously and is topologically stable. The surfaces of a sphere ($\chi = 2$) and torus ($\chi = 0$) are distinguished topologically by their Euler characteristics χ.

The earliest discovered topology-governed physical phenomenon was the celebrated quantum Hall effect[2–6]. In a two-dimensional electron system subject to low temperature and a strong magnetic field, the Hall resistance R_{xy} exhibits plateaus that take on quantized values $R_{xy} = h/ve^2$, with v being an integer number, e the elementary charge, and h the Planck's constant. The measured values of Hall conductance are integer or fractional (in the fractional quantum Hall effect[7,8]) multiples of e^2/h to nearly one part in a billion. Just like the Euler characteristic χ in mathematics, such a flat quantized resistance is related to the integer-valued integral of Berry curvature $\vec{F}$ over the filled portion of the bands in a crystal, the so-called Chern number, or TKNN number[4], $C = \frac{1}{2\pi}\int_{BZ}\vec{F}\cdot d\vec{S} \in \mathbb{Z}$. A most remarkable feature for such a topological nontrivial system is the celebrated bulk boundary correspondence, which indicates that the multiplicities of edge modes on the boundary are characterized by differences in the topological invariants of the bulk energy bands. A topologically protected surface state is guaranteed at the interface between two topologically distinct systems with $\Delta C = 1$, which possesses features of gaplessness, unidirectional propagation, and immunity to structural defects. Most early topological systems are found in the Hall effect family, e.g., quantum spin Hall effect[9–12], quantum anomalous Hall effect[13–15]. More detailed information can be found in previous reviews[16–18].

For a long time, research on topological physics had focused mainly on condensed-matter systems. In 2008, Haldane and Raghu[19,20] made the crucial generalization of topological physics into photonics by proposing that the presence of

*Address all correspondence to Shuang Zhang, shuzhang@hku.hk

"nonreciprocal" (Faraday-effect) media in photonic crystals can introduce a direct analog of the chiral edge states of electrons in the quantum Hall effect. The photonic bands would have nontrivial topological invariants in such an electromagnetic system. Shortly afterward, the idea was experimentally implemented by Wang *et al.* from MIT[21,22]. These works ushered in topological photonics research[23–34], which extended topological physics from quantum to classical systems. Similar ideas were later extended to other classical wave systems, e.g., acoustic waves, elastic waves[35–37]. Thus far, most studies on topological photonics have been implemented based on photonic crystals due to the similar principles between photonic crystals and electronic crystals. A number of recently published reviews have covered the development of the entire field[38–40].

This review will focus on another booming implementation in topological photonics based on metamaterials, especially the topological system at microwave frequencies based on three-dimensional metallic resonant structures. We will first briefly introduce some commonly used metamaterials in topological photonics and apply an RLC-based model (a circuit model consisting of a resistor, an inductor, and a capacitor) to describe its effective medium properties. Subsequently, an example is highlighted to show how particular constitutive relations could be connected to the topological property of the metamaterial. Following that, discussions on the metamaterial implementation of various photonic topological semimetals, i.e., Weyl point (WP), nodal line (NL), Dirac point (DP), and Yang monopole (YM) or Weyl surfaces, by introducing synthetic dimensions, will be presented. We will also briefly introduce some gapped topological systems, i.e., three-dimensional topological insulators (TIs) and the toroidal moment in k-space. Furthermore, a map is illustrated to show the connection between different topological phases. In addition, a comparison between the implementations of photonic crystals and metamaterials will also be discussed. Finally, we will discuss some perspectives and prospects of this research field.

2 Introduction to Metamaterials

Metamaterials are artificial structures composed of subwavelength resonators arranged in a certain spatial order. Since the interaction of resonators with light can be custom defined, the response of metamaterial is flexible and manipulable, resulting in a variety of novel physical phenomena, e.g., negative refraction, phase modulation, polarization control, and holograms. More detailed reviews of metamaterial can be found in Refs. [41–43].

Generally, metamaterials can be described by the effective medium model due to deep subwavelength unit cells, and the constitutive relation can be expressed in the most general formula

$$\begin{bmatrix} \vec{D} \\ \vec{B} \end{bmatrix} = \begin{bmatrix} \varepsilon_0 \boldsymbol{\varepsilon} & i\boldsymbol{\gamma}/c \\ -i\boldsymbol{\zeta}/c & \boldsymbol{\mu}_0 \boldsymbol{\mu} \end{bmatrix} \begin{bmatrix} \vec{E} \\ \vec{H} \end{bmatrix}. \tag{1}$$

Here, $\boldsymbol{\varepsilon}, \boldsymbol{\mu}, \boldsymbol{\gamma}, \boldsymbol{\zeta}$ are all 3×3 tensors, where $\boldsymbol{\varepsilon}$ and $\boldsymbol{\mu}$ are the relative permittivity and permeability tensors, respectively, and $\boldsymbol{\gamma}$ and $\boldsymbol{\zeta}$ are magneto-electric tensors. For a Hermitian system, they satisfy $\boldsymbol{\varepsilon}^\dagger = \boldsymbol{\varepsilon}, \boldsymbol{\mu}^\dagger = \boldsymbol{\mu}, \boldsymbol{\gamma} = \boldsymbol{\zeta}^\dagger$. These tensors can be engineered via the judicious design of resonator configurations.

Here, we briefly summarize some general properties of metamaterials.

A. In general, tensors $\boldsymbol{\varepsilon}$ and $\boldsymbol{\mu}$ are anisotropic. For example, a hyperbolic metamaterial[44,45] made of metallic wires behaves as a metal for E-field along the direction of metallic wires and as a dielectric along the other two directions, e.g., with $\varepsilon_{xx}, \varepsilon_{yy} > 0$ and $\varepsilon_{zz} < 0$. The equal frequency surface (EFS) of such a medium shows open hyperboloids, which allows a very large k-component, and facilitates potential applications, such as sensing or imaging[44–47].

B. Tensor $\boldsymbol{\gamma}$ describes the coupling between the electric field and magnetic field. In general, the trace of tensor $\mathrm{Tr}(\boldsymbol{\gamma})$ associated with diagonal terms γ_{ii} is called the chiral term or the bi-isotropic term[48,49], and the remaining terms (off-diagonal and zero-traced diagonal terms) indicate the bianisotropic terms[50,51]. For an isotropic chiral medium with $\gamma_{ii} = \gamma$, where $i = x, y, z$, the strong chirality lifts the degeneracy of the two circularly polarized states with the refractive indices $n_\pm = \sqrt{\varepsilon\mu} \pm \gamma$, which allows to achieve the negative refractive index without requiring simultaneous negative permittivity and negative permeability[49]. For example, magneto-electric coupling in the famous split-ring resonator (SRR) leads to the presence of a bianisotropic term, which was employed to realize transverse photon spin in a bulk medium[51].

C. Unlike photonic crystals, the constitutive relation is controlled mainly by the individual resonant units, so their spatial arrangement serves as an additional degree of freedom to control the wave propagation in the system. Recently, it has been used to control the local phase to realize wavefront modulation, holograms, etc., mainly in the 2D counterpart of metamaterials, the so-called metasurfaces[52,53]. Also, this degree of freedom can introduce various gauge fields into topological photonics[54].

An RLC-based model[55,56] is introduced to describe the constitutive relation induced by the resonant unit. For each metallic resonant unit, e.g., an SRR or a helix resonator, by considering the motion of electrons driven by external electromagnetic fields, the electromotive force can be written as

$$\begin{cases} U = -i\omega L \cdot I + \frac{q}{C} + IR, \\ U = \int \mathrm{d}\vec{l} \cdot \vec{E} - \int \mathrm{d}\vec{s} \cdot \partial\vec{B}/\partial t, \end{cases} \quad \text{and} \quad \begin{cases} I = \dot{q} = -i\omega q, \\ \partial\vec{B}/\partial t = -i\omega\mu_0 \vec{H}, \end{cases} \tag{2}$$

where the effective RLC circuit model consists of a resistor R, an inductor L, and a capacitor C. We have chosen the harmonic time-dependent term $\exp(-i\omega t)$. From the induced charge q and current I, we have the following expression for the electric/magnetic dipole responses:

$$\vec{p} = q \cdot \vec{S}_p = q \cdot \int \mathrm{d}\vec{l} \quad \text{and} \quad \vec{m} = -i\omega q \cdot \vec{S}_m = I \cdot \int \mathrm{d}\vec{s}. \tag{3}$$

Here, we introduce two column vectors $\vec{S}_p$ and $\vec{S}_m$ to represent the electric and magnetic dipole responses, respectively. Therefore, the electromotive force can be $U = (-\omega^2 L + 1/C - i\omega R)q = \vec{S}_p \cdot \vec{E} + i\omega\mu_0 \vec{S}_m \cdot \vec{H}$. With the effective RLC resonant frequency $\omega_0 = 1/\sqrt{LC}$ and effective loss $\Gamma = R/L$, the induced charge can be solved:

$$q = \frac{\vec{S}_p \cdot \vec{E} + i\omega\mu_0 \vec{S}_m \cdot \vec{H}}{L \cdot (\omega_0 - \omega^2 - i\omega\Gamma)}. \tag{4}$$

Therefore, considering a unit volume V, the polarization field $\vec{P}$ and magnetization field $\vec{M}$ are

$$\vec{P} = \frac{\vec{p}}{V} = \frac{\vec{S}_p(\vec{S}_p \cdot \vec{E}) + i\omega\mu_0 \cdot \vec{S}_p(\vec{S}_m \cdot \vec{H})}{LV \cdot (\omega_0 - \omega^2 - i\omega\Gamma)},$$
$$\vec{M} = \vec{m}/V = \frac{-i\omega\vec{S}_m(\vec{S}_p \cdot \vec{E}) + \omega^2\mu_0 \cdot \vec{S}_m(\vec{S}_m \cdot \vec{H})}{LV \cdot (\omega_0 - \omega^2 - i\omega\Gamma)}. \quad (5)$$

Inserting this equation into the constitutive relation $\vec{D} = \varepsilon_0\varepsilon_{\rm bg}\vec{E} + \vec{P}, \vec{B} = \mu_0(\mu_{\rm bg}\vec{H} + \vec{M})$, one can derive the material tensors as

$$\boldsymbol{\varepsilon} = \varepsilon_{\rm bg} \cdot I + \frac{\vec{S}_p\vec{S}_p}{\varepsilon_0 LV \cdot (\omega_0 - \omega^2 - i\omega\Gamma)},$$
$$\boldsymbol{\mu} = \mu_{\rm bg} \cdot I + \frac{(\omega/c)^2 \cdot \vec{S}_m\vec{S}_m}{\varepsilon_0 LV \cdot (\omega_0 - \omega^2 - i\omega\Gamma)},$$
$$\boldsymbol{\gamma} = \boldsymbol{\zeta}^\dagger = \frac{(\omega/c) \cdot \vec{S}_p\vec{S}_m}{\varepsilon_0 LV \cdot (\omega_0 - \omega^2 - i\omega\Gamma)}. \quad (6)$$

Here, the dyadic tensor $\vec{a}\,\vec{b} = a_i b_j \hat{e}_i \hat{e}_j$ denotes a 3×3 matrix. Thus, in such a medium with effective properties derived from the responses of individual resonant units, the effective $\boldsymbol{\varepsilon}, \boldsymbol{\mu}, \boldsymbol{\gamma}, \boldsymbol{\zeta}$ tensors are coupled and fully determined by the electric and magnetic dipole responses $\vec{S}_p$ and $\vec{S}_m$, respectively. A parallel configuration of the correlated electric and magnetic dipoles can induce the chiral response, while an orthogonal configuration enables the bianisotropic response. For example, $\vec{S}_p = \hat{e}_z$ ($\vec{S}_p = \hat{e}_y$) and $\vec{S}_m = \hat{e}_z$ introduce a nonzero γ_{zz} (γ_{yz}) term.

In general, a topological state can be linked to a particular constitutive relation. The degrees of freedom in metamaterials—27 in a Hermitian system and 54 in a non-Hermitian system—offer the possibility to realize specific topologies. For example, a chiral hyperbolic metamaterial corresponds to a Weyl semimetal, a medium with a perfect electromagnetic duality can function as a Dirac semimetal, and a medium with antisymmetric bianisotropy may serve as a TI. The following sections will describe each situation in detail.

It is worth mentioning that topological states are determined by certain combinations of the effective parameter tensors of the metamaterial, which in general cannot be realized by a single resonator. Quite often, the design of topological metamaterials requires a judicious combination of different resonant structures, e.g., $\vec{P} = (\sum_i \vec{p}_i)/V_{\rm tot}$ and $\vec{M} = (\sum_i \vec{m}_i)/V_{\rm tot}$. Therefore, although the response derives mainly from the resonant unit, analysis based on point/space groups is helpful to facilitate the design by canceling undesired electromagnetic responses. It is worth saying that the combination above can describe only a subwavelength state far from the Brillouin zone boundary, and a complete effective medium model fully consistent with the space group is still lacking.

The dispersion of such a dispersive medium is usually solved using the effective Hamiltonian method[57] by introducing auxiliary parameters to linearize the standard Maxwell equations. In this way, the Maxwell equations can be rewritten as an eigen problem for ω: $H(\vec{k})\Psi = \omega\Psi$. In addition, a more accurate model can be developed by considering the nonlocal effect induced by the interaction between adjacent units[58].

Indeed, once the corresponding constitutive relation is known, the $\boldsymbol{k} \cdot \boldsymbol{p}$ method can always be applied to obtain the approximate low-energy Hamiltonian near a topological degeneracy or a TI. For example, in a Weyl semimetal with a twofold degeneracy point, a standard method to obtain its low-energy Hamiltonian contains two steps. First, by solving the effective linear Hamiltonian $H(\vec{k})$ directly, a twofold degeneracy can be obtained, located at $[\vec{k}_{\rm WP}; \omega_{\rm WP}]$ with two eigenfunctions $\Psi_{\rm WP} = [\Psi_1, \Psi_2]$. Then using these eigenmodes as the basis and projecting the medium's full Hamiltonian matrix into this subspace, one can obtain a 2×2 $\boldsymbol{k} \cdot \boldsymbol{p}$ approximation (KPA) Hamiltonian to represent the low-energy Hamiltonian for a standard WP semimetal: $H_{\rm KPA}(\vec{k}) = \omega_{\rm WP} \cdot I + \Psi^\dagger_{\rm WP} \cdot [H(\vec{k}) - H(\vec{k}_{\rm WP})] \cdot \Psi_{\rm WP} = \omega_{\rm WP} \cdot I + \sum_{ij} v_{ij}\delta k_j \sigma_i$, with $\delta\vec{k} = \vec{k} - \vec{k}_{\rm WP}$.

3 Intrinsic Topology of Photons

While the original research on topological physical systems focused mainly on spin 1/2 electron fermionic systems, it has been shown that bosonic photons described by Maxwell equations could also have intrinsic topology[59,60]. In this section, we show how to separate the opposite topological charges subject to left/right circular polarization (LCP/RCP) and realize the nontrivial topological properties of photons.

In the Riemann–Silberstein (R-S) basis $\Psi_\pm = \frac{1}{\sqrt{2}}(\sqrt{\varepsilon_0} \cdot \vec{E} \pm i \cdot \sqrt{\mu_0} \cdot \vec{H})$, Maxwell's equation in vacuum can be expressed as two first-order equations:

$$i\vec{k} \times \Psi_\pm = \pm k_0 \Psi_\pm, \quad (7)$$

with $k_0 = \omega/c$. A cross product can be expanded using the Gell-Mann matrix, and the above eigen equation can be expressed in a standard formula:

$$H = k_x \cdot \lambda_x + k_y \cdot \lambda_y + k_z \cdot \lambda_z \quad \text{and} \quad H\Psi_\pm = \pm E\Psi_\pm, \quad (8)$$

with the relabeled Gell-Mann matrix defined as

$$\lambda_x = \begin{bmatrix} 0 & 0 & 0 \\ 0 & 0 & -i \\ 0 & i & 0 \end{bmatrix}, \quad \lambda_y = \begin{bmatrix} 0 & 0 & i \\ 0 & 0 & 0 \\ -i & 0 & 0 \end{bmatrix},$$
$$\lambda_z = \begin{bmatrix} 0 & -i & 0 \\ i & 0 & 0 \\ 0 & 0 & 0 \end{bmatrix}. \quad (9)$$

These operators obey the Lie algebra $[\lambda_i, \lambda_j] = i\varepsilon_{ijk}\lambda_k$. The relation is similar to that among the three Pauli matrices. This connection reveals the similarity between a fermionic spin 1/2 electron system and a bosonic spin-1 photon system. Indeed, Eq. (8) represents the minimal Hamiltonian of a standard threefold linear band degeneracy point that carries topological charge 2[61,62], and such a doubled charge directly describes a spin-1 quasiparticle.

From Eq. (8), e.g., for the Ψ_+ basis, it is convenient to solve the LCP/RCP eigenstates $e_\pm = \frac{1}{\sqrt{2}}(\vec{\theta} \pm i\vec{\phi}) \cdot \exp(i\phi_G)$ with eigenvalue $E = \pm k_0$, in which $\vec{\theta}$ and $\vec{\phi}$ are azimuthal and polar unit vectors, respectively, and ϕ_G is an arbitrary gauge phase. The photon has a linear dispersion in vacuum $\omega = \pm ck_0$, representing a massless particle located at the origin of momentum space $\vec{k} = 0$, as shown in Fig. 1(a). By parameterizing θ as the azimuth angle from k_z, the eigenstates $e_\pm = \frac{1}{\sqrt{2}}[-\cos\phi\cos\theta \pm i\sin\phi, -\sin\phi\cos\theta \mp i\cos\phi, \sin\theta] \cdot \exp(i\phi_G)$ are ill defined at either the north $\theta = 0$ or south $\theta = \pi$

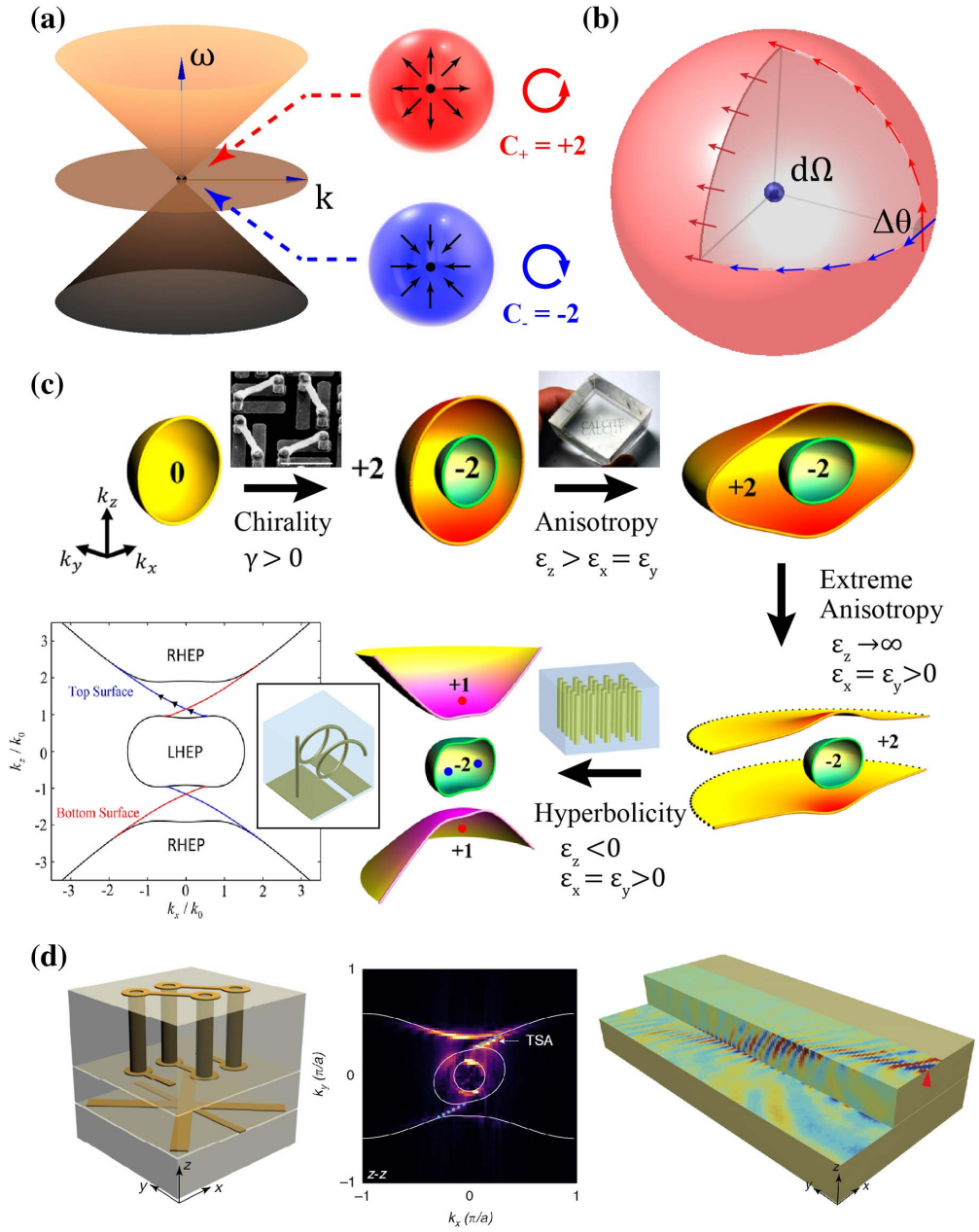

Fig. 1 (a) Linear dispersion (light cone) of the 3D "massless" photon $\omega = \pm ck$. At the origin of momentum space, i.e., $\vec{k} = 0$, there exists a magnetic monopole with the quantized Chern number $C_{L/R} = \pm 2$ for left/right circular polarization. (b) Schematic diagram of the geometric Berry phase; the parallel transport on a curved surface will accumulate a geometric phase of $\Delta\theta$ related to the solid angle dΩ. (c) Evolution of EFSs and their Chern numbers with additional chirality and hyperbolicity and the topologically protected surface states on the interface between chiral hyperbolic metamaterial and vacuum. (d) Realizable chiral hyperbolic metamaterial and topologically protected surface wave, whereas a backscattering-immune surface wave propagates across a three-dimensional step. (a) Adapted from [59], (c) from [63], and (d) from [64].

pole for a fixed ϕ_G—they are multivalued if we consider an adiabatic evolution process, despite the fact that ϕ cannot be defined at these poles, as both x and y coordinates are zero. Such discontinuous behavior is impossible to remove by choosing a particular gauge field or a specific coordinate system, which directly reveals the nontrivial intrinsic topology of such a photon system. Indeed, if we are able to find a gauge in which all wave functions are well defined, then the system cannot have a nontrivial topology.

This topology can be investigated by defining the magnetic flux in momentum space, i.e., Berry curvature: $\vec{F}_k = \nabla_k \times \vec{A}_k = \pm\vec{k}/k^3$, with $\vec{A}_k = -ie_\pm^\dagger \cdot \nabla_k e_\pm$. This curvature directly determines the accumulated geometric phase after the parallel transport through a closed path, $\Delta\theta = \int_{d\Omega} \vec{F} \cdot d\vec{S} = \pm d\Omega$,

as shown in Fig. 1(b). A Chern number is mathematically defined by an integral over an S^2 sphere that encloses the degeneracy point to represent the topological charge at $\vec{k} = 0$:

$$C_{\pm} = \frac{1}{2\pi}\int \vec{F}_k \cdot \mathrm{d}\vec{S} = \pm 2. \tag{10}$$

The magnetic monopole charge for the two circular polarization states is naturally quantized, $Q_{\pm} = \frac{1}{2}C_{\pm} = \pm 1$, which shows the intrinsic topology for bosonic photons. For completeness, there is one additional eigenstate $e_0 = \vec{k}/k$ for the eigenvalue $E = 0$, which possesses a vanishing Chern number $C_0 = 0$.

In a natural system, such a degeneracy point must be moved to a physically meaningful positive frequency with electric/magnetic resonances and longitudinal modes. However, despite the nontrivial topology of each circularly polarized state, degeneracy causes the topology of the overall system to remain trivial. Nevertheless, if these circularly polarized states can be separated in such a way that preserves their individual nontrivial topology, a topological phase with protected surface states would be expected[63–65].

This topological phase from the intrinsic topology of photons can be realized by transforming an isotropic system to a chiral hyperbolic system[63], as shown in Fig. 1(c). We start by introducing chirality γ, the diagonal $\boldsymbol{\gamma}$ matrix entries γ_{ii}, by employing helical structures as unit cells. It lifts the degeneracy of the two circularly polarized waves with different effective refractive indices $n_{\pm} = \sqrt{\varepsilon\mu} \pm \gamma$; therefore, the Chern number of the outer/inner EFS is $\pm 2 \cdot \mathrm{sgn}(\gamma)$. Such a process reveals the intrinsic topology of the two circularly polarized states. However, to fully separate these two states with a complete gap in momentum space, an additional anisotropy item $\varepsilon_z \neq \varepsilon_x = \varepsilon_y$ is introduced. As shown in Fig. 1(c), both EFSs are elliptically distorted, with the outer one experiencing a more significant deformation, i.e., the EFS is more flattened with very large in-plane wave vectors. An extreme anisotropy with ε_z approaching infinity will break the outer EFS into two pieces, with each one sharing half of the total Chern number. Considering positive and negative infinities as the same point, further pushing ε_z through infinity to a finite negative value while keeping $\varepsilon_x = \varepsilon_y$ fixed, i.e., by incorporating some metallic wires into the unit cell, these two sheets are deformed into two hyperboloids, completely separated from the original inner EFS by a gap. This chiral hyperbolic metamaterial thus displays three well separated and topologically nontrivial EFSs, with $C_{\mathrm{up}} = C_{\mathrm{lower}} = \mathrm{sgn}(\gamma)$ and $C_{\mathrm{center}} = -2\,\mathrm{sgn}(\gamma)$. The topologically nontrivial EFSs are expected to be bridged by equifrequency surface arcs, at surfaces of certain orientations. Notably, the spatial separation of left- and right-moving surface waves at a given k_z prevents backscattering from any z-invariant disorder.

Experimental observation of such a photonic topological system[64] was implemented using the unit cell shown in Fig. 1(d). It was constructed by stacking up two functional layers: a layer consisting of an array of metallic wires along the y direction to introduce the desired hyperbolic properties, and a layer consisting of metallic helices to introduce chirality and break the inversion symmetry (IS) [left panel of Fig. 1(d)]. Additional metallic crosses are superimposed on the wires to suppress the nonlocal effects. Such a photonic metamaterial supports a topologically protected surface state. In the experiment, a near-field measurement directly maps out both the amplitude and phase of the field on the surface of the metamaterial. A Fourier transform of the measured complex field provides the EFS in momentum space, which agrees well with the simulation results [middle panel of Fig. 1(d)]. In addition, the surface wave propagation across a step formed by the metamaterial is measured. There is no reflection across the step, serving as direct visualization of the robustness of the topological surface states [right panel of Fig. 1(d)]. It is worth mentioning that this chiral hyperbolic metamaterial is indeed a type-II Weyl system[65,66], and the observed nontrivial topological property originates from WPs hosted by the system, which will be discussed in the next section.

4 Weyl Semimetals in Metamaterials

WPs play a key role in topological physics. WPs[67] refer to the isolated degeneracy points in 3D momentum space with a linear band crossing, i.e., 3D extension of the 2D DPs in graphene. In electronic systems, one of the most well-known material systems that host WPs is the TaAs family (TaAs, TaP, NbAs, NbP)[40,68–70]. Close to the WPs, the effective Hamiltonian involves only two bands and takes the general form $H = \omega_0 \cdot I + \sum_i \xi_i(\vec{k}) \cdot \sigma_i$, with σ_i being Pauli matrices that obey both the Lie algebra $[\sigma_i, \sigma_j] = i\varepsilon_{ijk}\sigma_k$ and Clifford algebra $\{\sigma_i, \sigma_j\} = 2\delta_{ij}$. Without any particular symmetry, the band crossing submanifold determined by three $\xi_i = 0$ conditions must be three dimensions lower than the crystal's dimension, which guarantees the existence of a 0D WP in 3D momentum space. Around such a degeneracy point, $\xi_i(\vec{k})$ takes a simple form of $\xi_i(\vec{k}) = \sum_j v_{ij}k_j + O(k^2)$ after a standard Taylor expansion process. Therefore, the low-energy Hamiltonian of standard Weyl degeneracy reads

$$H = \omega_0 \cdot I + \sum_{i,j} v_{ij}k_j\sigma_i. \tag{11}$$

This Hamiltonian shows a strong resemblance to the triple degeneracy points located at $\vec{k} = 0$ discussed in the previous section. Such a degeneracy point is topologically stable because any perturbation $\Delta H = a \cdot \sigma_i$ can shift only the location of WPs in momentum space but cannot lift the degeneracy. The topology of the WP is characterized by the Berry curvature and Chern number. Each standard WP carries an integer Chern number:

$$C_{\mathrm{WP}} = \mathrm{sgn}[\det(\boldsymbol{v})] = \pm 1. \tag{12}$$

This integer topological invariant called chirality implies a magnetic monopole charge $Q_{\mathrm{WP}} = \frac{1}{2}C_{\mathrm{WP}} = \pm\frac{1}{2}$ located at the degeneracy point. Therefore, the only way to break the degeneracy is to merge and annihilate two WPs carrying opposite topological charges. For a particular isotropic WP with $v_{ij} = \pm v_0\delta_{ij}$, the magnetic monopole serves as the source (or drain) of Berry curvature:

$$\vec{F}_{\mathrm{WP}} = Q_{\mathrm{WP}} \cdot \frac{\vec{k}}{k^3}. \tag{13}$$

Consider the constraints of Berry curvature under different symmetries:

$$\vec{F}(\vec{k}) = +\vec{F}(-\vec{k}) \quad \text{with IS},$$
$$\vec{F}(\vec{k}) = -\vec{F}(-\vec{k}) \quad \text{with time-reversal symmetry (TRS)}. \quad (14)$$

There will be no WP when both IS and TRS are present. A Weyl semimetal must break either or both of them. Also, the famous Nielsen–Ninomiya no-go theorem[71–74] dictates that WPs in a crystal have to appear in pairs with $\sum_i C_i = 0$. Therefore, the minimal number of WPs with broken IS or TRS is four or two, respectively.

The bulk boundary correspondence of the topologically nontrivial chiral characteristic predicts the existence of topologically protected Fermi arcs[75], which connect two WPs with opposite chiralities, as shown in Figs. 2(a) and 2(b). Consider a cylinder in the Brillouin zone whose axis is perpendicular to the surface; if the cylinder surrounds one WP with Hamiltonian $H = \sum_i v_i k_i \sigma_i$, then the Hamiltonian $H = H(\theta, k_z) = v_x k_r \cos\theta \cdot \sigma_x + v_y k_r \sin\theta \cdot \sigma_y + v_z k_z \cdot \sigma_z$ can be interpreted as the 2D Chern insulator for a nonzero fixed k_r parameter. The two parameters $[\theta, k_z]$ define the surface of the cylinder, which further can be regarded as a torus due to the periodic boundary condition along k_z in momentum space. Berry curvature integration gives the Chern number of such a 2D Chern insulator, which is determined by summation of the chiralities of the WPs enclosed within the cylinder. With a boundary at $z = 0$, there must exist a chiral edge state for this subsystem, which crosses zero energy at a certain critical θ. This state can be obtained for every cylinder enclosing only a single WP. Thus, a topologically protected arc terminates at two WPs with opposite chiralities, the so-called Fermi arc, which serves as one of the key fingerprints of Weyl systems.

The aforementioned chiral hyperbolic media[63,64] are photonic Weyl semimetals, as shown previously[65]. One can generate either a type-I or type-II WP[80–82] by controlling the nonlocal effect of the longitudinal mode. A chiral hyperbolic medium has TRS but lacks IS. Indeed, there are two negative WPs wrapped by the center EFS, and the upper/lower EFS each encloses a single positive WP, as shown in Fig. 1(c). These WPs are responsible for the nontrivial EFSs with $C \neq 0$, and the topologically protected surface state arcs connect the projections of these bulk EFSs.

Apart from this, WPs of various forms have been proposed and realized in bosonic or fermionic systems[23,26,30,83–85]. A recently published review about Weyl semimetals in condensed matter systems can be found in Ref. [40]. However, a complicated configuration of energy bands at the Weyl energy is unsuitable for research or applications. In particular, some highly intriguing effects, such as helicoidal surface states[76,86] and chiral anomaly[87–89], may not be favored in these Weyl systems.

In 2018, Yang *et al.* proposed an ideal Weyl system based on a photonic metamaterial setup[76,77], as shown in Figs. 2(c) and 2(d). All Weyl nodes are symmetry related, residing at the same energy with a significant momentum separation and devoid of nontopological bands in a sufficiently large energy interval. Such a meta-crystal exhibits four WPs, the minimum number allowed in the presence of TRS, and a symmorphic space group $P\bar{4}m2$ (No. 115) is used to guarantee the existence and location of the four ideal WPs.

The designed photonic ideal Weyl semimetal consists of periodically buried saddle-shaped metallic coils in a dielectric substrate, as shown in the inset of Fig. 2(d). Further analysis of the electromagnetic response reveals that the unit can be viewed as two orthogonal SRRs that behave like two resonant inclusions in each unit cell. The electromagnetic dipolar responses of these two resonators can be approximately expressed as

$$\begin{cases} \vec{S}_{p,\mathrm{red}} = [0, l, 0]^T, \\ \vec{S}_{m,\mathrm{red}} = [A, 0, 0]^T, \end{cases} \quad \text{and} \quad \begin{cases} \vec{S}_{p,\mathrm{blue}} = [l, 0, 0]^T, \\ \vec{S}_{m,\mathrm{blue}} = [0, A, 0]^T. \end{cases} \quad (15)$$

A and l are the effective area and length of the resonators, respectively. Therefore, the effective medium model in Eq. (9) exhibits the symmetric bianisotropic effect $\gamma_{xy} = \gamma_{yx} \neq 0$, leading to a direction-dependent chirality response, which breaks IS. The unavoidable crossings between the longitudinal mode with negative dispersion (due to the nonlocal effect) and the transverse mode with positive dispersion along $\Gamma - \mathrm{M}$ form a type-I WP. The other three WPs are related to it by the D_{2d} symmetry operations of the structure. The space group symmetry guarantees that these four Weyl nodes are all located on $\Gamma - \mathrm{M}$ at the same frequency, and any two adjacent WPs carry opposite chiralities.

Yang's paper studies the helicoidal structure[76,86] of the surface state arcs by applying near-field scanning measurement. The measured EFSs, as shown in Fig. 2(e), exhibit four symmetrically displaced elliptical bulk projections, and two surface state arcs run across the Brillouin zone boundaries and bridge the neighboring bulk projections with opposite chiralities. With the increase in frequency, the top surface arc rotates anticlockwise/clockwise, depending on the chirality of the WP where it emerges. Around 13.5 GHz, a transition occurs with the surface arc connection changing into a new configuration: a direct surface arc connected between the bulk states within the Brillouin zone and a surface ellipse centered at its edge. The surface ellipse and surface arcs together form the unified helicoid surface in the dispersion of the surface states.

Such an ideal Weyl semimetal system can also serve as a perfect photonic platform for exploring other intriguing effects of WPs, such as chiral anomaly[54], and developing possible topological devices, such as vortical reflection[90], spiraling Fermi arcs[90], and Veselago lenses[91].

Here, we only briefly introduce the realization of chiral anomaly based on this ideal Weyl semimetal system[54,92], as shown in Figs. 2(f) and 2(g). Chiral anomaly[87–89] is an important signature associated with the chirality of WPs. Weyl systems can support one-way chiral zero modes under a strong magnetic field with non-conservative chiral currents. This can be realized by introducing a pseudo magnetic field via engineering the space-dependent shift of degeneracy points in momentum space[93,94]. Rotating the metallic coil with a tiny angle θ causes the angular shift of WPs around the Γ point, which can be considered as the artificial gauge field: $\vec{k}_{\mathrm{WP}} = \vec{k}_{\mathrm{WP},0} + \vec{A}_{\mathrm{WP}}$. Taking the WP Q1 as an example and setting rotation angle θ as a linear function of the spatial coordinate $\theta = ax$, one can approximately define the gauge field:

$$\vec{A}_{\mathrm{WP}}(x) = \Delta\vec{k}_{\mathrm{WP}}(x) \approx [1, -1, 0] \cdot ax \cdot |\vec{k}_{\mathrm{WP},0}|/\sqrt{2}. \quad (16)$$

This gauge field implies an artificial magnetic field: $\vec{B} = B_z \hat{e}_z = -a \cdot |\vec{k}_{\mathrm{WP},0}|/\sqrt{2} \cdot \hat{e}_z$. In the experiment, such an artificial magnetic field can reach $477m^{-2}$. For clockwise rotation, the direction of the generated artificial magnetic field for each WP can be along either z or $-z$ direction. Determined by

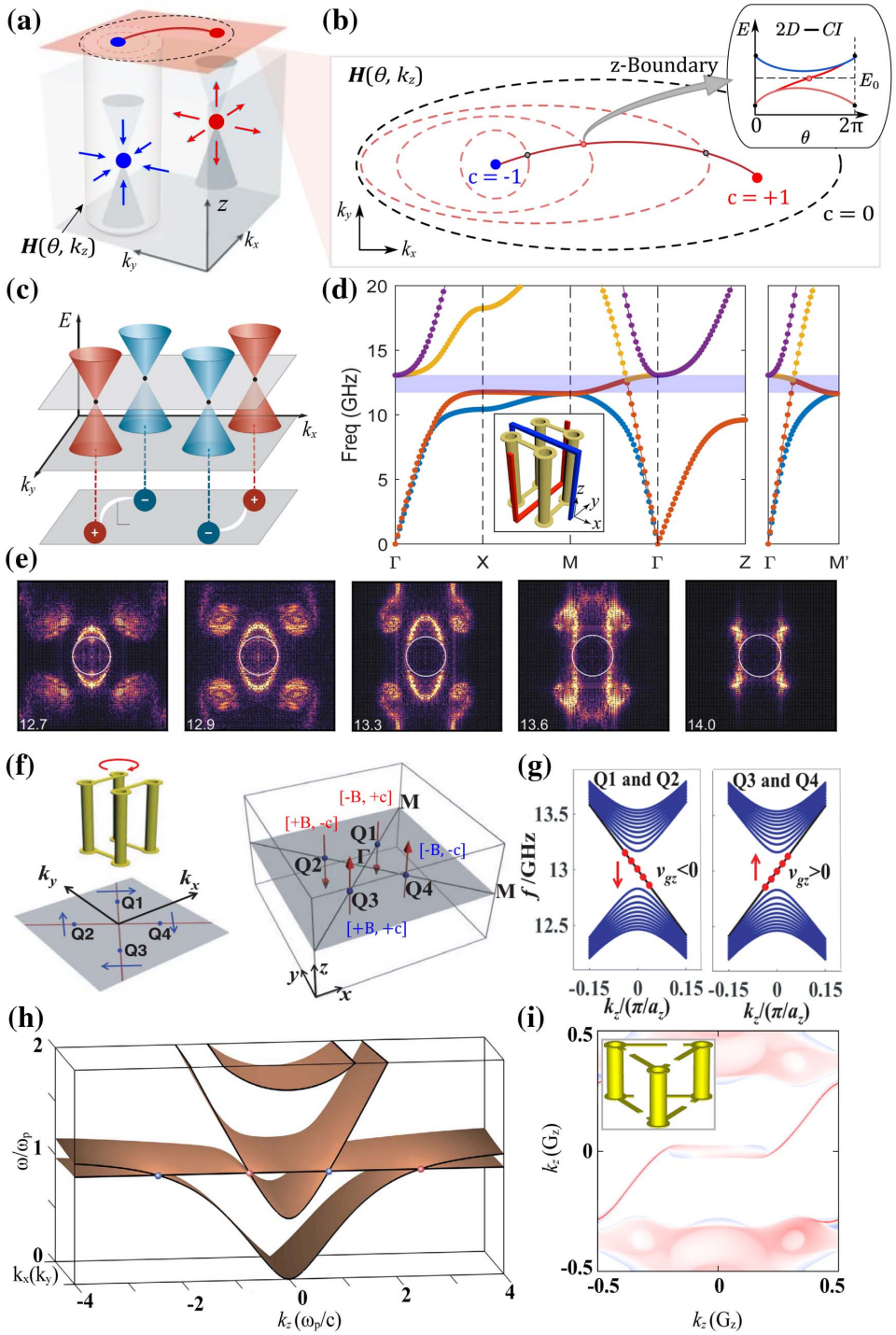

Fig. 2 (a) Schematic diagram of WPs and the Fermi arcs. (b) Intrinsic topologically protected Fermi arcs connect two WPs with opposite chiralities. (c), (d) Structure and band topology of the ideal photonic Weyl metamaterial. (e) Experimental EFSs of the topological helicoidal surface states. (f), (g) A pseudo-gauge field generated by the space-dependent rotation angle supports a zeroth-order chiral Landau level with one-way propagation in ideal Weyl semimetals. (h) Dispersion spectrum of plasmonic WPs in magnetized plasma with time-reversal symmetry (TRS) broken. (i) Unit structure and EFS of an ideal unconventional Weyl semimetal in a chiral photonic metamaterial with $C = \pm 2$. (c)–(e) Adapted from [76,77], (f), (g) from [54], (h) from [78], and (i) from [79].

both the directions of the artificial magnetic fields and the chiralities of WPs, the zeroth Landau levels for WPs Q3 and Q4 have positive group velocities along the z direction. In contrast, WPs Q1 and Q2 have chiral zero modes with negative group velocity. This k-dependent one-way propagation was experimentally verified.

In addition to the aforementioned Weyl semimetal with broken IS by chiral or bianisotropic terms, photonic Weyl semimetals can also be realized with broken TRS in a naturally existing medium—magnetized plasma: free electron gas under a static bias magnetic field[78,95]. This magnetized plasma can also be described as an effective medium. The cyclotron frequency can exceed the plasma frequency when the applied magnetic field is strong enough, which results in crossings between the longitudinal plasmon mode and helical propagating modes at the plasma frequency, as shown in Fig. 2(h). These crossing points are WPs responsible for all non-vanishing Berry curvature and nontrivial topological features[78]. The experimental observation of such photonic Weyl degeneracy is implemented in a magnetized semiconductor InSb at the terahertz band[95]. Ideal Weyl semimetals with broken TRS were also experimentally realized in 3D magnetic photonics crystals[96], or in an ultracold atom system by engineering 3D spin–orbit coupling[97], which includes only two WPs, the minimum number of WPs in a crystal.

There are also some unconventional Weyl semimetals that may carry topological Chern numbers of two or higher[61,62,98–101], e.g., a Hamiltonian reads

$$H = \begin{bmatrix} v_\perp \cdot k_z & v_\parallel \cdot (k_x - ik_y)^N \\ v_\parallel \cdot (k_x + ik_y)^N & -v_\perp \cdot k_z \end{bmatrix}, \qquad N \in \mathbb{Z}. \quad (17)$$

This Hamiltonian implies a Chern number $C = \pm N$. It possesses different properties from the standard charge-1 WPs, including multiple Fermi arcs that stretch over a large portion of the Brillouin zone, as shown in Fig. 2(i) in a photonic metamaterial implementation[79].

5 Nodal Line Semimetals in Metamaterials

NL semimetals[102] contain band crossings in the form of one-dimensional rings in the Brillouin zone of a 3D crystal. CaP_3 and $SrIrO_3$ are examples of such NL semimetals[103,104]. Such a double degeneracy must satisfy the three conditions $\xi_i(\vec{k}) = 0$, $i = 1, 2, 3$ discussed in the above sections. Therefore, the presence of an NL semimetal must be protected by extra spatial symmetries, such as mirror, inversion, glide, or screw symmetries, which reduces the number of practical constraints[102]. The NL may transform into other topological states by introducing spin–orbit coupling or a lowered crystal symmetry. A significant feature of the NL is that an eigenstate adiabatically transported along with a closed π_1 loop threading the NL accumulates $\pm\pi$ Berry phase, leading to a Zak phase difference between the inside and outside of the NL[105]. Like Weyl semimetals, NL semimetals are also accompanied by surface states, the so-called drumhead surface states, characterized by surface bands embedded inside the surface projections of bulk NLs. However, these surface states are not robust, which means a small perturbation can destroy the surface bands[106,107].

A photonics NL semimetal was first predicted by Lu *et al.*[23] based on a double-gyroid photonic crystal. Apart from this, one of the first realized NL semimetals in the metamaterial context is an I-shaped metamaterial[108] satisfying the space group *P*4/*mbm* (No. 127), as shown in Figs. 3(a)–3(c). The structure consists of two mutually orthogonal I-shaped metallic cut-wire resonators lying in the x–y plane. The electromagnetic responses of these two I-shaped metallic cut-wires with effective length l can be approximately expressed as

$$\vec{S}_{p,\pm} = \frac{1}{\sqrt{2}} \cdot [l, \pm l, 0]^T \quad \text{and} \quad \vec{S}_{m,\pm} = [0, 0, 0]^T. \quad (18)$$

Along the in-plane $\vec{k}$ directions, the lowest three bands are formed by two transverse modes and a longitudinal bulk plasmon (LP) mode. The orthogonality between LP and transverse electric (TE) modes is guaranteed by the mirror symmetry (M_z) of the system. The 2D band structure confirms the ring degeneracy between LP and TE modes when $k_z = 0$. Through spatial Fourier transformations of the scanned near-field distributions, both the bulk and surface states of the NL semimetal were observed.

In such a metamaterial, the nonlocal effect[112], which induces the negative slope of the LP mode, plays a key role in the formation of NL semimetals. This nonlocal effect can be involved in the effective medium model by considering a modified k-dependent effective length: $l(\vec{k}) = l_0 \cdot \sqrt{1 - \alpha \cdot (k_x^2 + k_y^2)}$, where α is a constant indicating the modulation strength. It is worth saying that if the dielectric layer is replaced by a gyro-electric material that breaks TRS, the NL semimetal would be gapped everywhere except for at two isolated points along the applied magnetic field, which are identified as WPs. Such a transformation from WPs to an NL or vice visa can always be realized through a tuned space group with lowered symmetry.

A similar NL semimetal in metamaterial[109] is shown in Figs. 3(d)–3(f), in which the structure satisfies space group *P*4/*nbm* (No. 125). The unit resonator is similar to the aforementioned design in the ideal WP system but in a different space group with IS. The degeneracy forms an NL protected by glide symmetry. Interestingly, this NL semimetal possesses an hourglass-shaped band structure, where the line degeneracies cannot be annihilated while preserving all underlying spatial symmetries, in contrast to the previous one arising from accidental degeneracy between two bands with opposite mirror eigenvalues.

To describe such an NL semimetal located at the Brillouin zone boundary with $k_z = \pi/p_z$, a direct constitutive relation obtained from Section 2 is insufficient due to the lack of periodic structures and a Brillouin zone. A space-group-based analysis would be more appropriate. The lattice contains three glide mirror operations involving a half-lattice translation: M_x: $(x, y, z) \mapsto (-x, y + 1/2, z)$, M_y: $(x, y, z) \mapsto (x + 1/2, -y, z)$, and M_z: $(x, y, z) \mapsto (x + 1/2, y + 1/2, -z)$. The bands located on the Brillouin zone boundaries of the $k_z = \pi/p_z$ plane, e.g., an arbitrary P point in Fig. 3(e), are all doubly degenerate due to the anticommutation relations $\{M_z, M_y\} = 0$ ($\{M_z, M_x\} = 0$) when $k_y = \pi/p_y$ ($k_x = \pi/p_x$). Such a condition ensures that states $|\psi\rangle$ and $M_y|\psi\rangle$ ($M_x|\psi\rangle$) can be two degenerate eigenstates of the M_z operator, but with opposite eigenvalues. However, at the Z point with $\vec{k} = [0, 0, \pi/p_z]$, the little group D_{4h} ensures that two degenerate pairs belong to two higher irreducible representations E_u and E_g, which possess M_z eigenvalues 1 and -1, respectively. On the whole $k_z = \pi/p_z$ plane, M_z symmetry is preserved, and thus any states on this

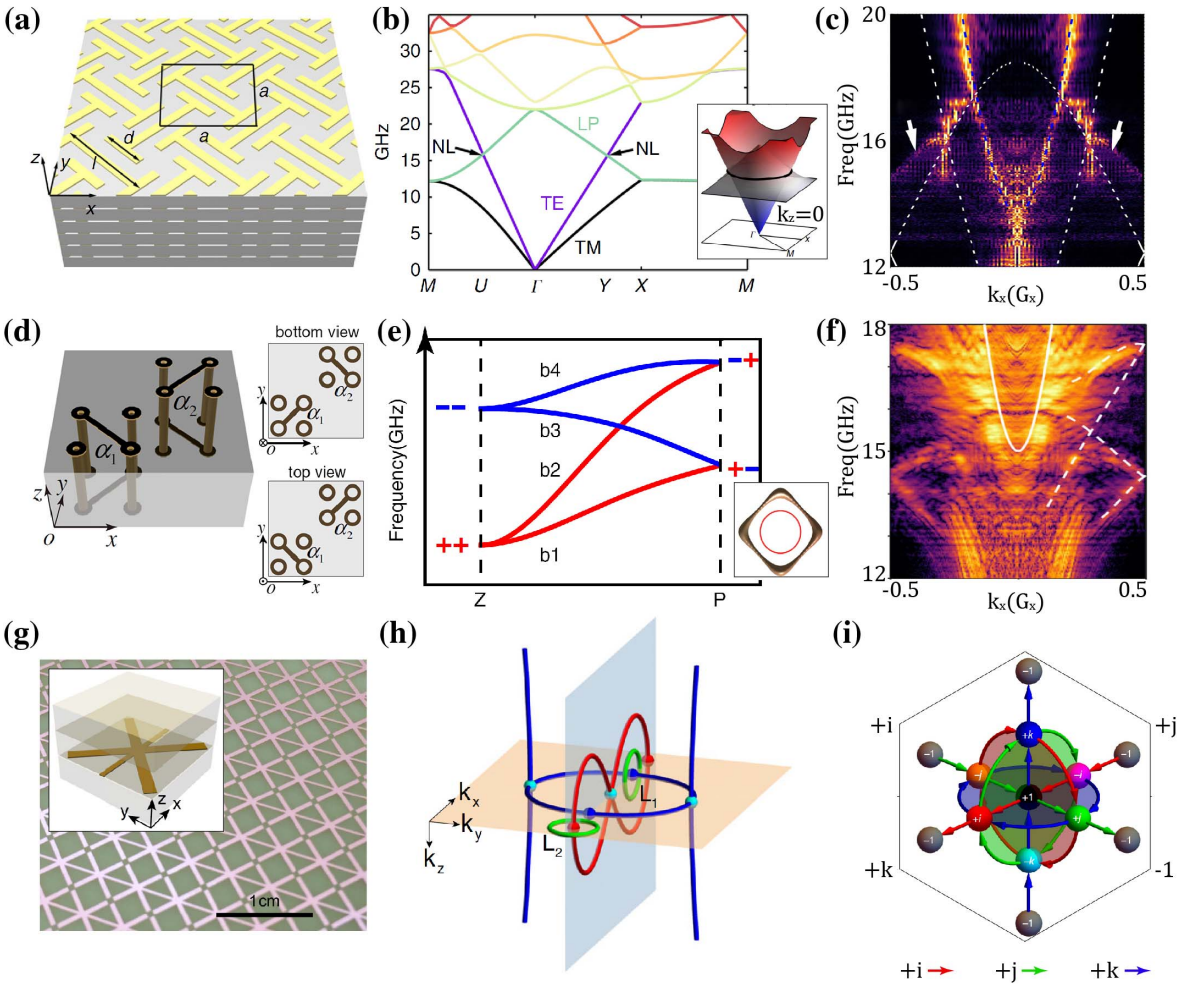

Fig. 3 (a) Unit of an I-shaped metamaterial satisfying the space group *P*4/*mbm* (No. 127). (b) Simulated band structure along high symmetry lines. (c) The measured bulk and surface dispersions identify a single nodal ring in the metamaterial. (d)–(f) Similar to (a)–(c), but for another metamaterial configuration satisfying space group *P*4/*nbm* (No. 125). (g) Biaxial hyperbolic metamaterial belonging to space group *Pmmm* (No. 47). (h) Nodal link structure in the metamaterial. (i) Graphical representation of the quaternion group $\mathbb{Q}$ and associated non-Abelian group multiplications. (a)–(c) Adapted from [108], (d)–(f) from [109], (g), (h) from [110], and (i) from [111].

plane can be labeled by the eigenvalue of M_z. Therefore, the states with the same eigenvalue of M_z must be connected, as shown in Fig. 3(e), which constructs hourglass-shaped band dispersion with an inevitable intersection. As P can freely move along the Brillouin zone boundaries, a photonic hourglass NL is located on the $k_z = \pi/p_z$ plane. A similar hourglass NL was recently proposed in the phonon spectra of natural materials[113].

Another design of NL metamaterial[110] is shown in Figs. 3(g) and 3(h), which can also be transformed from the WP metamaterial[64] shown in Fig. 1(d) by removing the chiral part. This metamaterial can be described by a biaxial hyperbolic effective medium with $\boldsymbol{\varepsilon} = \mathrm{diag}([\varepsilon_x, \varepsilon_y, \varepsilon_z])$, where all three ε_i are different from each other. Due to the TRS and IS, multiple NLs occur, located on the high-symmetry mirror planes, that is $k_i = 0$, with $i = x, y, z$. The most significant feature is the mutually linked structures. As a consequence, closed loops that encircle a blue (red) NL formed between the upper (lower) two bands both accumulate $\pm\pi$ Zak phases, accompanied by evolutions for different eigenstates. Globally, they are described by the non-Abelian quaternion group $\mathbb{Q}$[114], where $\mathbb{Q} = [\pm i, \pm j, \pm k, \pm 1]$, with anticommuting imaginary units satisfying $ij = -ji = k$ and $i^2 = j^2 = k^2 = -1$, as shown in Fig. 3(i). The sign of the charge assigns an orientation to the nodal links, and topological charge -1 indicates a loop encircling two NLs with the same orientations and color. It is topologically distinct to the trivial class 1, which can be smoothly shrunk to a single point without touching any NLs. These non-Abelian quaternion charges possess non-commutative and rich braiding structures with multiple bandgaps tangled together, which impose additional constraints on the admissible NL transitions. Recently, there has been growing attention paid to NLs with special non-Abelian braiding features and topological charges. In a transmission line network, these non-Abelian topological charges are observed through the eigenstate-frame

sphere, and the non-Abelian bulk boundary correspondence has been observed[111,115].

6 Dirac Point and High-Dimensional Degeneracy in Metamaterials

Similar to WPs, DPs[116] in a 3D crystal are also the linear crossing points of energy bands but with fourfold degeneracy. Dirac semimetals Na_3Bi and Cd_3As_2 were the first experimentally confirmed 3D topological semimetals[117,118]. Dirac semimetals bridge conventional insulators, TIs, and Weyl semimetals. It is equivalent to overlapping two WPs with opposite topological charges in momentum space. It may be split into two individual WPs with opposite chiralities through breaking either TRS or IS. Thus, the standard Hamiltonian of a massless DP can be block diagonalized: $H_D = \mathrm{diag}(H_W, H_W^*)$, with $H_W(\vec{k}) = \sum_i k_i \sigma_i$ representing a standard WP. Consequently, the Chern number for a DP is always zero, but at the interface between air and DP, there are still spin-dependent (or mode-dependent) topological surface states, and the Fermi arcs from the two individual WPs are formed in different eigenstate subspaces.

A uniaxial metamaterial can be designed to realize a 3D photonic DP by introducing resonance in both the permittivity and permeability along the axis[119,120]. The simplest effective medium takes the formulas $\boldsymbol{\varepsilon} = \mathrm{diag}(1, 1, \varepsilon_{zz})$ and $\boldsymbol{\mu} = \mathrm{diag}(1, 1, \mu_{zz})$, with the perfect electromagnetic duality $\varepsilon_{zz} = \mu_{zz} = 1 - \omega_p^2/\omega^2$ (similar for the identical Lorenz-type dispersions). In this system, the two degenerate transverse modes (LCP/RCP) and the two degenerate LP modes ($E_z \pm i \cdot H_z$) cross each other at a pair of symmetric points $[\pm\vec{K}_D; \omega_D] = [0, 0, \pm k_D; \omega_p]$, with $k_D = \omega_p/c$. Near these fourfold degeneracy points, the effective Hamiltonian has the form

$$H_D = \omega_{k0} \cdot I + \sum_{i=1}^{3} v_i k_i \cdot \Gamma_i, \tag{19}$$

with Γ_i indicating the Dirac matrices $\vec{\Gamma} = [-\sigma_0\tau_1, \sigma_3\tau_2, \sigma_0\tau_3]$ satisfying the Clifford algebra $\{\Gamma_i, \Gamma_j\} = 2\delta_{ij}$. This Hamiltonian covers the standard DP form except for the additional tilt and shift terms.

The metamaterial design[119,120] for realizing such a uniaxial constitutive relation is shown in Figs. 4(a) and 4(b). The unit cell consists of a set of metallic helices satisfying D_{4h} group symmetry. The metallic helices with $S_{p,z} \neq 0$ and $S_{m,z} \neq 0$ introduce both electric and magnetic resonances along the z direction. Also, the mirror and C_4 rotation symmetries eliminate all the chiral and bianisotropic responses. Therefore, the D_{4h} group symmetry ensures that both $\boldsymbol{\varepsilon}$ and $\boldsymbol{\mu}$ take the form of the uniaxial tensor. The duality of ε_{zz} and μ_{zz} is realized by the precisely adjusted structural parameters effectively with $|S_{p,z}| = k_D \cdot |S_{m,z}|$. The duality symmetry[122] protects the DPs in such a metamaterial. Spin-dependent Fermi arcs are experimentally observed in such a Dirac semimetal metamaterial, as shown in Fig. 4(c).

As a gapless topological phase, a Dirac semimetal serves as a parent topological phase that can lead to various interesting topological phases, e.g., TIs, Weyl semimetals, and NLs, through symmetry reduction. Such a DP can also be extended to a higher-dimensional topological structure by introducing additional synthetic dimensions[121].

Mathematically, for the Hermitian matrix of rank four, there are exhaustively five gamma matrices satisfying the Clifford algebra $\{\Gamma_i, \Gamma_j\} = 2\delta_{ij}$, with $\Gamma_{1,2,3}$ given in Eq. (19), and additional $\Gamma_4 = \sigma_2\tau_2$, $\Gamma_5 = \sigma_1\tau_2$[123]. Therefore, in 5D space, there exists a gapless Hamiltonian:

$$H_Y = \omega_{k0} \cdot I + \sum_{i=1}^{5} v_i k_i \cdot \Gamma_i, \tag{20}$$

which represents the fourfold degeneracy point, the so-called YM[124,125]. Three of the gamma matrices can couple with the 3D wave vectors, and the remaining two matrices can couple with two material parameters, which can be further treated as two additional synthetic dimensions. They altogether form a 5D space. Here we choose the bianisotropic terms γ_{xz} and γ_{yz} as the two material parameters. For a judiciously designed medium with the above uniaxial metamaterial and a purely antisymmetric chiral matrix, $\gamma_{zx} = -\gamma_{xz}$, $\gamma_{zy} = -\gamma_{yz}$, the medium below behaves like a 5D YM with $k_4 = \omega_p\gamma_{xz}$ and $k_5 = \omega_p\gamma_{yz}$[121]:

$$\hat{\boldsymbol{\varepsilon}} = \begin{bmatrix} 1 & & \\ & 1 & \\ & & 1 - \frac{\omega_p}{\omega^2} \end{bmatrix}, \quad \hat{\boldsymbol{\mu}} = \begin{bmatrix} 1 & & \\ & 1 & \\ & & 1 - \frac{\omega_p}{\omega^2} \end{bmatrix},$$
$$\hat{\boldsymbol{\gamma}} = \begin{bmatrix} & & \gamma_{xz} \\ & & \gamma_{yz} \\ -\gamma_{xz} & -\gamma_{yz} & \end{bmatrix}. \tag{21}$$

The Hamiltonian H_Y satisfies TP symmetry (T is time-reversal symmetry and P is space-inversion symmetry) with $T = i\sigma_2\tau_0 K$ (K is the complex conjugation) and $(TP)^2 = -1$, and possesses a globally doubly degenerate linear band structure near the YM. By defining a $U(2)$ Berry connection, one can calculate its non-Abelian second Chern number $C_2^{\mathrm{NA}} = \pm 1$.

The nonzero synthetic momentum components can be introduced to the original Dirac metamaterial by adjusting the geometry and orientation of each column of helices via breaking the C_4 symmetry. First, each helix should be precisely adjusted, where an additional constraint $S_{p,y}S_{m,z} + S_{p,z}S_{m,y} = 0$ should be satisfied for the approximate helix responses $\vec{S}_p = [0, S_{p,y}, S_{p,z}]$ and $\vec{S}_m = [0, S_{m,y}, S_{m,z}]$. Second, each pair of helices satisfying mirror symmetry should be precisely rotated to the angles $\Phi_{1\mapsto 4} = \psi_{45} + 45° + [\delta_{45}, \delta_{45} + 90°, -\delta_{45} + 180°, -\delta_{45} + 270°]$. Finally, the synthetic momentum components can be introduced to realize a 5D YM metamaterial:

$$\hat{\boldsymbol{\gamma}} \propto \frac{S_{m,y}}{S_{m,z}} \cdot \begin{bmatrix} 0 & 0 & \cos\psi_{45} \\ 0 & 0 & \sin\psi_{45} \\ -\cos\psi_{45} & -\sin\psi_{45} & 0 \end{bmatrix} \cdot \sin\delta_{45}. \tag{22}$$

A realistic metamaterial design based on the above discussion is shown in Fig. 4(d).

A YM in 5D space is not topologically stable because Γ matrices do not satisfy the Lie algebra $[\Gamma_i, \Gamma_j] \neq i\varepsilon_{ijk}\Gamma_k$. A YM can transform into linked Weyl surfaces[126–128] by a general perturbation item $\Delta H = a \cdot \Gamma_{mn}$, with $\Gamma_{mn} = i/2 \cdot [\Gamma_m, \Gamma_n]$ ($m \neq n$). Such a perturbation can be added to the YM Hamiltonian by other material parameters, such as magneto-optic effects,

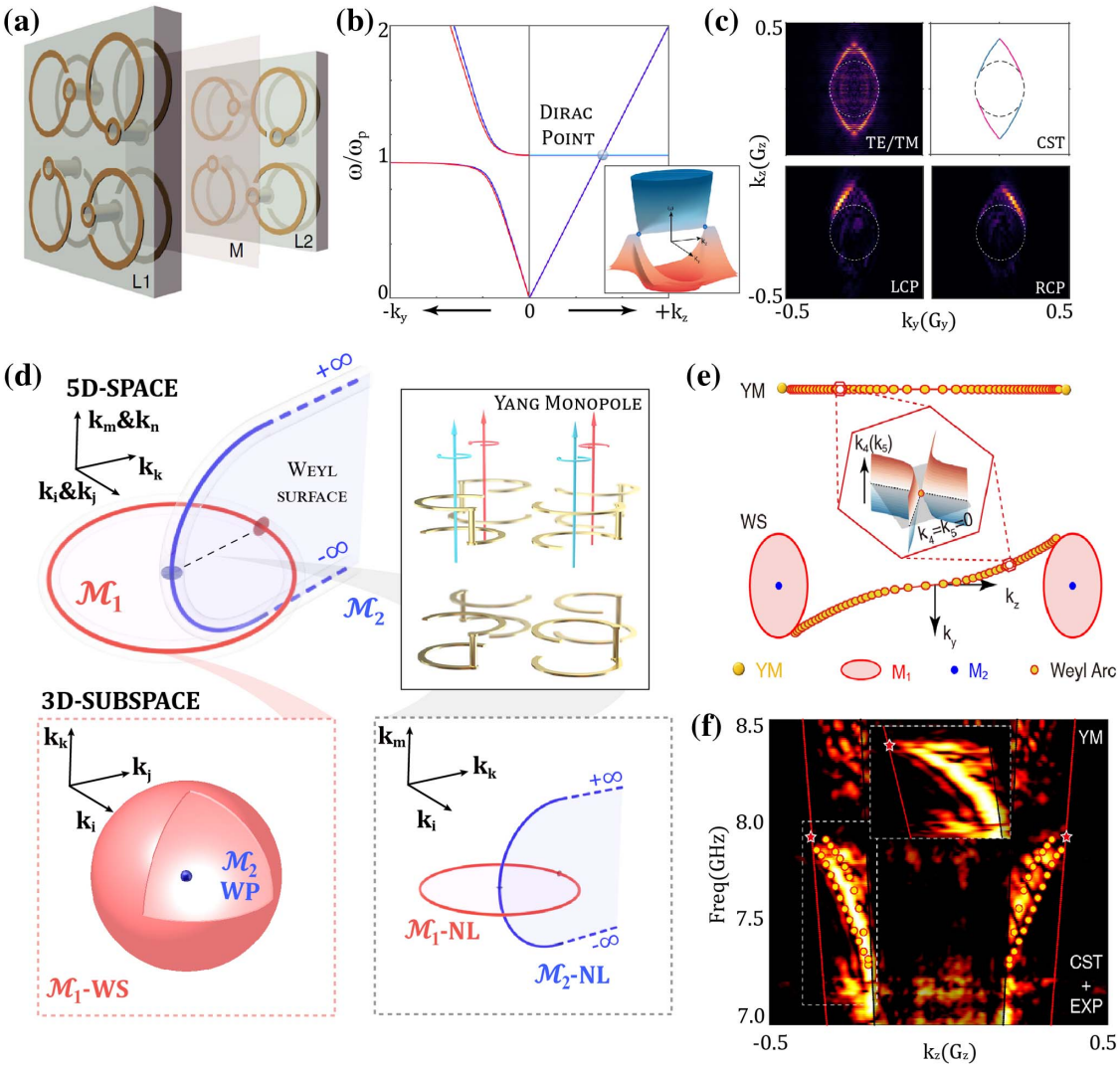

Fig. 4 (a) Schematic of the 3D photonic Dirac metamaterial, with each unit cell consisting of eight helical elements satisfying D_{4h} point symmetry. (b) Dispersions along k_y (k_z). (c) Spin-dependent Fermi arcs identify the DP in such a metamaterial. (d) Modified 5D YM metamaterial with introducing additional synthetic k_4 and k_5 dimensions and 5D k-space (3D k-subspace) distributions of the linked WSs perturbed from the YM metamaterial. (e) 1D Weyl arcs for both a system with YM and that with Weyl surfaces. (f) Simulated and measured dispersions of surface states along k_z direction for YM metamaterial. (a)–(c) Adapted from [119,120] and (d)–(f) from [121].

chiralities, and anisotropic items[121]. The degenerate manifold is called the Weyl surface because any point on the degenerate two manifolds serves as a WP in the corresponding three-codimension subspace orthogonal to the nodal surface. The Abelian second Chern number C_2^A of these two manifolds is the same as the non-Abelian one in the original YM system: $C_2^A|_{\mathrm{WS}} = C_2^{\mathrm{NA}}|_{\mathrm{YM}} = \pm 1$. This global topological invariant describes the linking number of these Weyl surfaces. The manifestation of this linking property in a particular 3D subspace is the wrapping of WPs by a degeneracy ellipsoid or linked NLs, as shown in Fig. 4(d), which was experimentally verified[121]. Importantly, such a higher-dimensional structure provides a unified view of different topological phases in lower dimensions, such as WPs, NLs, and DPs.

The topological bulk boundary correspondence in a 5D YM or Weyl surface system is manifested by 3D Fermi hypersurfaces and 1D Weyl arcs at the 4D boundaries of these 5D nontrivial systems[126]. The "Weyl" property protects the 3D Fermi hypersurface by a nontrivial first Chern number defined in 3D subspace. Similar to the discussion for the Fermi arc shown in Fig. 2(b), any cross section with fixed k_z located between (outside) the two YMs corresponds to a 4D gapped system with $|C_2| = 1$ (0). Such a system with nontrivial C_2 is known to exhibit the 4D quantum Hall effect and host surface states with surface WPs[129]. By gradually shifting k_z between two YMs of opposite C_2, the WPs form a 1D arc, i.e., Weyl arc, extending from one YM/Weyl surface to the other, as shown in Fig. 4(e). This high-dimensional topologically protected Weyl arc is experimentally observed in a YM system, as shown in Fig. 4(f).

It is worth mentioning that an antisymmetric bianisotropic matrix can provide synthetic dimensions not only in the YM and linked Weyl surface systems but more universally in general

electromagnetic media. With the help of the Pauli and Gell-Mann matrices, for a medium with antisymmetric bianisotropic matrices, i.e., $\boldsymbol{\gamma} = -\boldsymbol{\gamma}^T$. Maxwell equations can be formulated in an elegant form:

$$[(\omega\gamma_{xy}\sigma_x - k_z\sigma_y)\cdot\lambda_2 - (\omega\gamma_{zx}\sigma_x - k_y\sigma_y)\cdot\lambda_5 + (\omega\gamma_{yz}\sigma_x - k_x\sigma_y)\cdot\lambda_7]\cdot\Psi_{EH} = \omega\cdot\frac{1}{2}[(\sigma_0+\sigma_z)\cdot\varepsilon_0\hat{\boldsymbol{\varepsilon}} + (\sigma_0-\sigma_z)\cdot\mu_0\hat{\boldsymbol{\mu}}]\cdot\Psi_{EH}. \quad (23)$$

Here, λ_2, λ_5, and λ_7 are the three antisymmetric Gell-Mann matrices, and $\Psi_{EH} = [E, H]^T$. Therefore, $\varepsilon_{mnp}k_p$ and $\omega\gamma_{mn}$ are on equal footing for a general medium with arbitrary $\boldsymbol{\varepsilon}$ and $\boldsymbol{\mu}$.

In the 3D subspace of natural wave vectors, these synthetic dimensions provided by material parameters function as effective mass, which also corresponds to spin–orbit coupling terms in some papers[122]. These terms induce a bandgap at the degeneracy point in 3D space; thus, the system behaves like a TI, discussed in the next section. Indeed, a TI can always be considered a cross section of a higher-dimensional topological semimetal. Thus, a TI is connected to a higher-dimensional semimetal through the dimension reduction process, e.g., the connection between a 2D Chern insulator and a 3D WP[75].

7 Topological Gapped Systems in Metamaterials

In the previous sections, we discussed a number of photonic metamaterial semimetals, including WP, NL, and DP semimetals, in three dimensions, and YM and Weyl surfaces in five dimensions. This section will briefly introduce the 3D gapped system based on metamaterials, including photonic TIs[130] and momentum space toroidal moments (MTMs)[131], which can be derived from the introduction of effective mass terms into 3D DP and NL semimetals, respectively.

A 3D photonic TI[130] is shown in the right panel of Fig. 5(a), which arises from the aforementioned 3D DP metamaterial shown in the left panel. The designed DP metamaterial in a triangular lattice consists of six connected SRRs distributed with mirror symmetries M_z and at an angle of 120° apart in the x–y plane. The back-to-back arrangement of the SRRs cancels the bianisotropy. Thus, for the fine-tuned lattice parameters, 3D frequency-isolated DP occurs at K and K' points. A 3D TI is

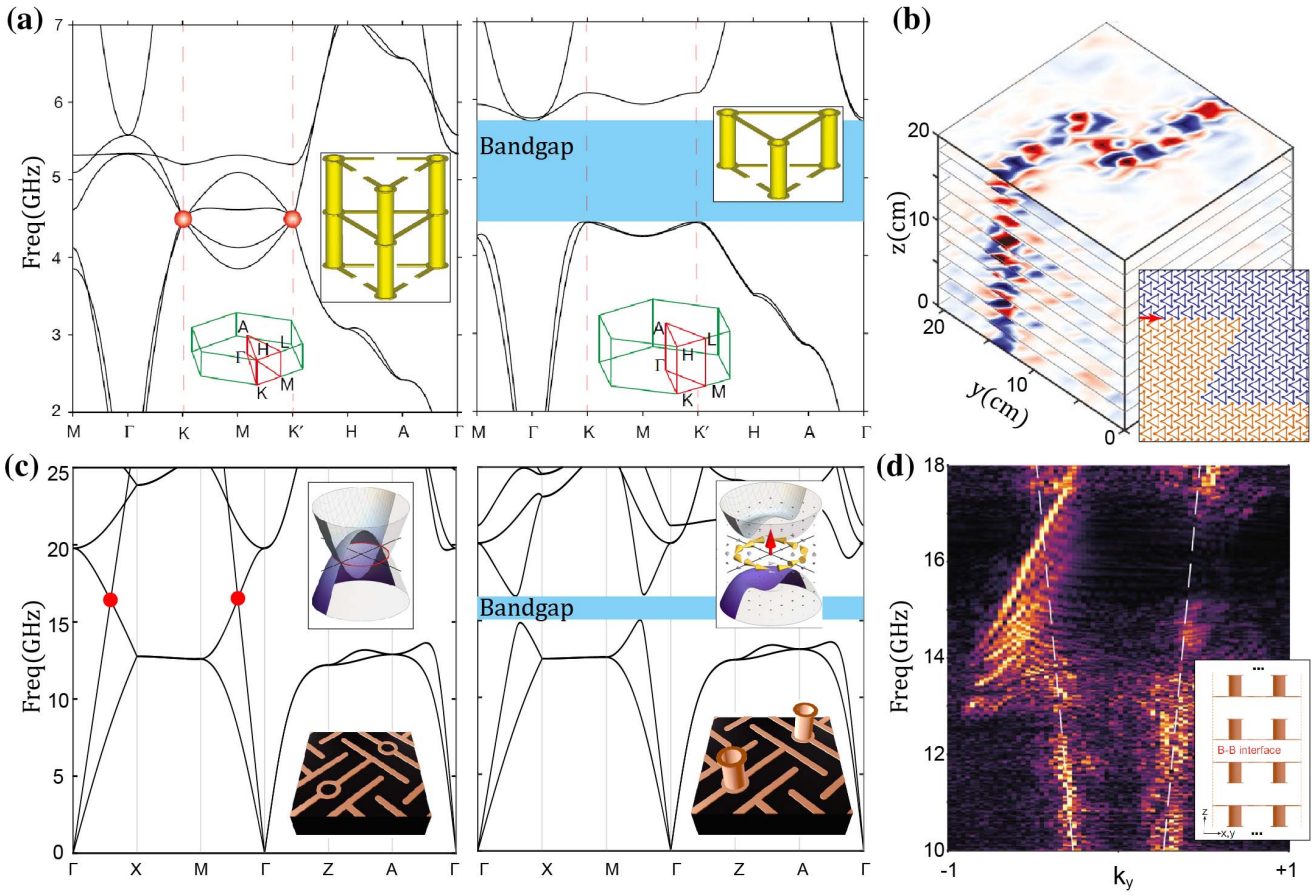

Fig. 5 (a) Band structures along high symmetry lines for (left panel) 3D gapless DP and (right panel) gapped TI, where the complete bandgap is shadowed. Inset: corresponding photonic metamaterial unit with/without breaking M_z mirror symmetry. (b) Experimental demonstration of the robustness of photonic surface states between TIs with the opposite mass terms. (c) Similar to (a), but for a 3D NL and fully gapped NL exhibiting Berry curvature vortex. (d) Experimentally mapped interface states between back-to-back MTMs. (a), (b) Adapted from [130] and (c), (d) from [131].

proposed by removing the upper/lower three SRRs. This adjustment breaks the mirror symmetry M_z and induces a net antisymmetric bianisotropic term $\gamma_{xy} = -\gamma_{yx}$, which behaves as a mass term $m \cdot \Gamma_4$ to the original DP Hamiltonian $H = \omega_{k0} I + \sum_{i=1}^{3} v_i \cdot (k_i - K_{i,0}) \cdot \Gamma_i$ and opens the bandgap. The sign of the mass term depends on the orientation of the three saved SRRs[132]. This resonance-enhanced bianisotropy allows for a topological bandgap with a width greater than 25%, which exceeds previously demonstrated topological bandgap widths in 2D (less than 10%) and 3D (a few percent or incomplete) proposals.

Topological internal domain wall states flowing robustly along with the interface between two TIs with opposite mass terms were demonstrated in microwave experiments. Such a robust photonic transport was detected even around sharp corners (sharply twisted, with two 60° corners), as shown in Fig. 5(b). It is worth saying that the aforementioned 5D YM metamaterial can be considered as such a 3D TI with nonzero synthetic momenta.

A toroidal moment has the configuration of a ring formed by magnetic fields[133,134]. The concept can also be extended to momentum space, i.e., an MTM formed by a ring of a Berry curvature field. A photonic metamaterial's MTM[131] is shown in Fig. 5(c) (inset of right panel), where Berry curvature shows a 3D vortex distribution. This MTM can be derived from the aforementioned NL metamaterial[108], as shown in Fig. 3(a), by introducing a small metallic bar in the vertical direction to slightly break the mirror symmetry M_z. The effective resonator response can be transformed from Eq. (18) to

$$\vec{S}_{p,\pm} = \frac{1}{\sqrt{2}} \cdot [l, \pm l, 0]^T \quad \text{and} \quad \vec{S}_{m,\pm} = \frac{1}{\sqrt{2}} \cdot [-A, \mp A, 0]^T. \tag{24}$$

This configuration is equivalent to two mutually perpendicular SRRs. The nonzero magnetic response introduces an additional antisymmetric bianisotropic term $\gamma_{xy} = -\gamma_{yx}$ to the original NL metamaterial, as in the case of TI. This term behaves as a rotationally invariant mass term $m\sigma_y$ added to the original NL Hamiltonian $H = (k_x^2 + k_y^2 - a) \cdot \sigma_z + k_z \cdot \sigma_x$. The direction of the metallic bar determines the sign of this mass term. As we know, a quantized π Berry phase is accumulated along the π_1 loop threading the gapless NL. Thus, for a sufficiently small bandgap, this Berry curvature, i.e., the effective magnetic field in momentum space, is tightly concentrated around the original NL ring to form the MTM. It is a polar toroidal dipole moment $T \propto \int \vec{k} \times \Omega(\vec{k}) \mathrm{d}\vec{k}$[135] with Berry flux approaching positive or negative π, depending on the sign of the mass term.

Helical domain-wall states are experimentally observed at the interfaces between two MTM metamaterials with opposite mass terms, which show either positive or negative dispersion, depending on the orientations of the metamaterials. The bulk and surface states are experimentally investigated with "back-to-back" configurations, as shown in Fig. 5(b). This phenomenon can be interpreted as a 3D valley Hall system[136]. On any arbitrary cutting plane containing the rotation axis, such as the k_y–k_z plane, the integration of Berry curvature over half of the 2D Brillouin zone (e.g., $k_y > 0$) approaches π for a small enough bandgap. Therefore, interface states run through the gap and show gapless features, serving as evidence of the toroidal configuration of Berry curvature distribution.

8 Connections between Different Topological States

In the previous sections, we discussed case-by-case 3D/5D topological semimetals and insulators based on 3D metallic resonant structures at microwave frequencies. The different topological states addressed above can transit from one to another by introducing/breaking specific symmetries, e.g., TRS or IS, and by considering a dimension reduction process. A map is shown in Fig. 6 to illustrate the topological phase transition on the metamaterial platform.

In a 5D system, a YM semimetal and a Weyl surface semimetal can transform into each other by introducing/breaking the TP-symmetry operator $(TP)^2 = -1$, where both topological states have the same nontrivial second Chern number $C_2 = \pm 1$. By considering a dimension reduction process from 5D to 3D, a DP semimetal can derive from the YM semimetal, while WP semimetals and NL semimetals can result from the Weyl surface semimetal by locally considering only two bands and preserving different symmetries[121]. An NL semimetal can be converted to a WP semimetal by breaking TRS through a magnetic field[108], or by breaking IS through a chiral structure or a modified space group, as shown in Refs. [64,76,109,110]. Furthermore, a DP semimetal is formed by overlapping two WPs at different bands by simultaneously preserving TRS and IS[119,120]. In addition, TIs can be converted from the corresponding semimetals by adding a mass term—an antisymmetric bianisotropic term, e.g., transition from a DP semimetal to a four-band TI[130], and from an NL semimetal[108] to an MTM[131]. It is worth noting that the transition from a WP semimetal to a two-band TI is an exception. The only way to break the degeneracy is to merge and annihilate two WPs carrying opposite topological charges[96].

9 Topological Photonic States in Non-metamaterial Systems

It should be noted that almost all the mentioned topological semimetals/insulators can also be realized with judiciously engineered photonic crystal systems. Indeed, a photonic WP semimetal was first realized in a double-gyroid photonic crystal at microwave frequencies by Lu *et al.*[23,26] with broken IS. WP semimetals were also realized in optical lattices[137,138], superlattices[139], synthetic parameter spaces[140], Floquet networks[141,142], and circuits[143–145]. NL semimetals[23,146–149], Dirac semimetals[27,150–152], and TIs[153–156] were also demonstrated using photonic crystals made from dielectric materials. Similar topological states can also be realized in dielectric metamaterials at higher frequencies[151] or in 2D metamaterials[157].

However, there is a key difference between photonic crystals and metamaterials, in that the former controls mainly the dispersion via the near-field coupling between unit cells or the interference between the scattered fields from unit cells, and uses spatial modes as the basis, while the latter realizes the desired dispersion primarily by the resonance effect of individual unit cells, with the effective polarization states as the basis.

In a photonic crystal, dispersion is determined mainly by the space group, and the degeneracy points are usually located at high symmetry points/lines. An advantage for a photonic crystal implementation is a reduced Ohmic loss at optical frequencies by using all-dielectric components. However, complex space group structures for the design of photonic crystals often imply complex unit cell structures, e.g., the double-gyroid photonic crystal[23,26]. These units are generally challenging to be

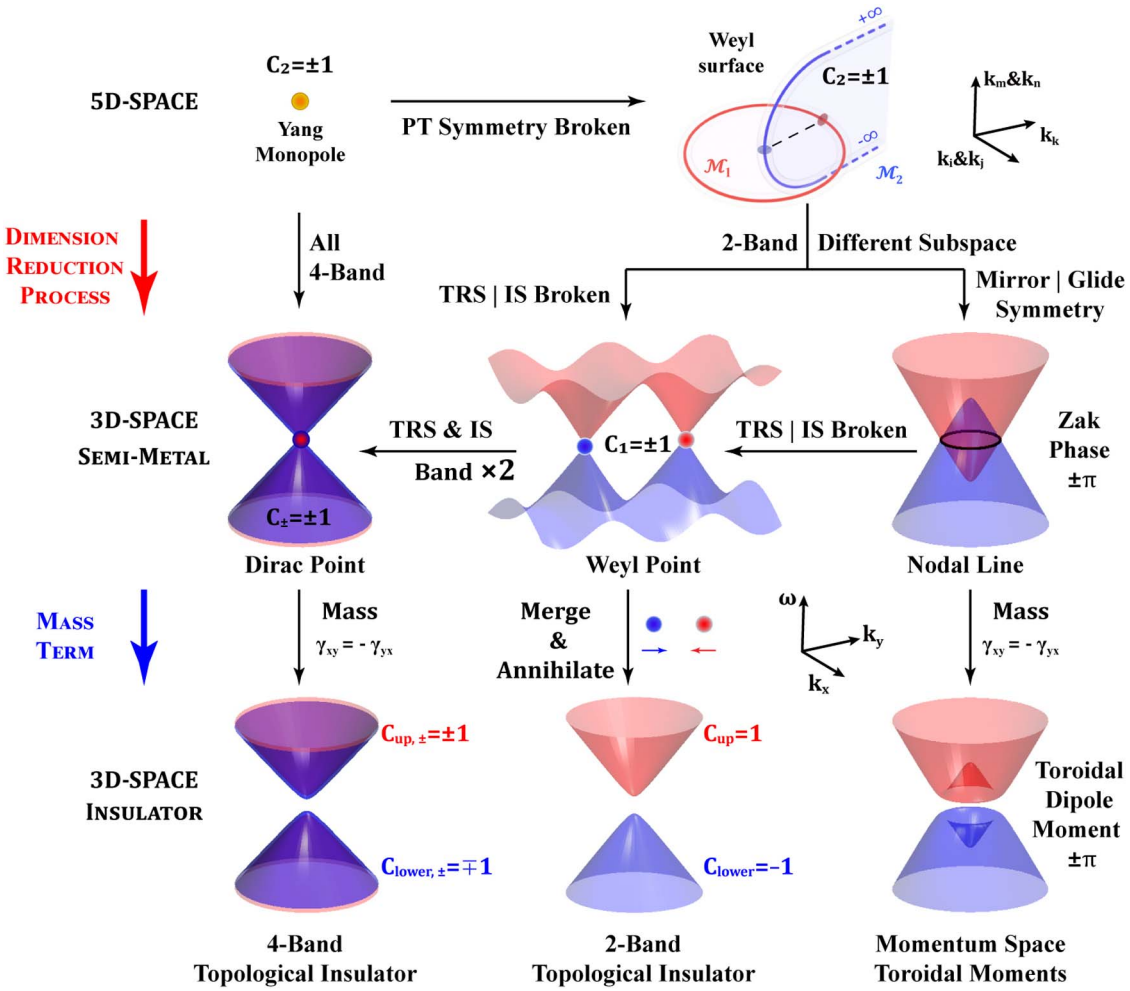

Fig. 6 Illustration of the topological phase transition on the metamaterial platform.

compatible with the planar manufacturing process and need to be prepared by solutions such as 3D printing[158].

With metamaterials, the deep subwavelength unit cell allows the use of the effective medium model to describe their electromagnetic responses. As such, the constitutive relation determines the underlying topological property. On the other hand, the effective medium description of the metamaterial electromagnetic properties is also dependent on the space group. The ability to adjust dispersion can be allocated to both the resonance of individual unit cells and the interaction between them. Compared to photonic crystals, the deep-subwavelength unit cells of metamaterials provide the following advantages: (1) due to the large size of the Brillouin zone, the surface states can be designed to be sufficiently away from the bulk states, leading to more tightly confined surface states; (2) the resonance-based functionality (instead of interference based, as in the case of photonic crystals) provides better tolerance to disorders, as shown in Refs. [159,160]. The degrees of freedom in the spatial arrangement can be employed to introduce various gauge fields.

10 Conclusion and Perspectives

In this review, we focus mainly on the metamaterial implementations of several gapless and gapped topological phases in photonics. Each topological state can be linked to a particular constitutive relation that can be transformed into realistic metamaterial designs. These topological states can also transit into each other by imposing or breaking specific symmetries. The metamaterial that achieves a particular constitutive relationship can be designed by considering both the electromagnetic resonance responses of metallic resonators and extra point/space groups. Hence, topological analysis of the electromagnetic properties of metamaterials provides a new powerful platform to achieve some complex electromagnetic wave control. It is worth saying that while the RLC-based model works well in studying dispersion and the topological properties of metamaterials, a more refined model that incorporates point/space group analysis provides a more powerful means for designing metamaterials.

Looking forward, there are many possible exciting directions in this field.

A. The extension of topological metamaterial to other classical wave systems, such as elastic systems[161,162]. Although this has been done with the crystal concept, a metamaterial (effective) approach may lead to a more straightforward analysis of topological properties.

B. The search for possible applications of topological metamaterials. Topological metamaterial provides new possibilities

for light manipulation, which holds promise for novel devices and applications, e.g., one-way topological fiber[163] and Veselago lensing[91,164].

C. Photonic metamaterial opens doors to the study of topological phases in various synthetic dimensions, e.g., by introducing various artificial gauge fields and pseudo electric/magnetic fields. They can be used to explore some elusive phenomena, including high-dimensional chiral anomaly[87,88,165], quantum oscillation[166,167], wormhole effect[168], and other effects arising from non-Abelian gauge fields[169,170] in photonic metamaterial systems.

D. Investigation of non-Hermitian systems[171,172], hyperbolic lattices[173], time crystals[174], Anderson insulators[175], and high-order topological systems[176–178] with photonic metamaterial platforms.

Acknowledgments

This work was supported by the Horizon 2020 Action Projects (648783 (TOPOLOGICAL), 734578 (D-SPA), and 777714 (NOCTORNO)) and the Research Grants Council of Hong Kong (AoE/P-502/20).

References

1. A. Hatcher, *Algebraic Topology* (Cambridge University Press, 2002).
2. K. V. Klitzing, G. Dorda, and M. Pepper, "New method for high-accuracy determination of the fine-structure constant based on quantized hall resistance," *Phys. Rev. Lett.* **45**, 494 (1980).
3. R. B. Laughlin, "Quantized Hall conductivity in two dimensions," *Phys. Rev. B* **23**, 5632 (1981).
4. D. J. Thouless et al., "Quantized Hall conductance in a two-dimensional periodic potential," *Phys. Rev. Lett.* **49**, 405 (1982).
5. K. S. Novoselov et al., "Room-temperature quantum Hall effect in graphene," *Science* **315**, 1379 (2007).
6. M. E. Cage et al., *The Quantum Hall Effect* (Springer Science & Business Media, 2012).
7. D. C. Tsui, H. L. Stormer, and A. C. Gossard, "Two-dimensional magnetotransport in the extreme quantum limit," *Phys. Rev. Lett.* **48**, 1559 (1982).
8. G. Moore and N. Read, "Nonabelions in the fractional quantum Hall effect," *Nucl. Phys. B* **360**, 362 (1991).
9. C. L. Kane and E. J. Mele, "Z_2 topological order and the quantum spin Hall effect," *Phys. Rev. Lett.* **95**, 146802 (2005).
10. C. L. Kane and E. J. Mele, "Quantum spin Hall effect in graphene," *Phys. Rev. Lett.* **95**, 226801 (2005).
11. B. A. Bernevig, T. L. Hughes, and S.-C. Zhang, "Quantum spin Hall effect and topological phase transition in HgTe quantum wells," *Science* **314**, 1757 (2006).
12. B. A. Bernevig and S.-C. Zhang, "Quantum spin Hall effect," *Phys. Rev. Lett.* **96**, 106802 (2006).
13. C.-X. Liu et al., "Quantum anomalous Hall effect in $Hg_{1-y}Mn_yTe$ quantum wells," *Phys. Rev. Lett.* **101**, 146802 (2008).
14. C.-Z. Chang et al., "Experimental observation of the quantum anomalous Hall effect in a magnetic topological insulator," *Science* **340**, 167 (2013).
15. Y. Deng et al., "Quantum anomalous Hall effect in intrinsic magnetic topological insulator $MnBi_2Te_4$," *Science* **367**, 895 (2020).
16. M. Stone, *Quantum Hall Effect* (World Scientific, 1992).
17. H. L. Stormer, D. C. Tsui, and A. C. Gossard, "The fractional quantum Hall effect," *Rev. Mod. Phys.* **71**, S298 (1999).
18. J. Sinova et al., "Spin Hall effects," *Rev. Mod. Phys.* **87**, 1213 (2015).
19. F. D. M. Haldane and S. Raghu, "Possible realization of directional optical waveguides in photonic crystals with broken time-reversal symmetry," *Phys. Rev. Lett.* **100**, 013904 (2008).
20. S. Raghu and F. D. M. Haldane, "Analogs of quantum-Hall-effect edge states in photonic crystals," *Phys. Rev. A* **78**, 033834 (2008).
21. Z. Wang et al., "Reflection-free one-way edge modes in a gyromagnetic photonic crystal," *Phys. Rev. Lett.* **100**, 013905 (2008).
22. Z. Wang et al., "Observation of unidirectional backscattering-immune topological electromagnetic states," *Nature* **461**, 772 (2009).
23. L. Lu et al., "Weyl points and line nodes in gyroid photonic crystals," *Nat. Photonics* **7**, 294 (2013).
24. M. C. Rechtsman et al., "Photonic Floquet topological insulators," *Nature* **496**, 196 (2013).
25. L. Lu, J. D. Joannopoulos, and M. Soljačić, "Topological photonics," *Nat. Photonics* **8**, 821 (2014).
26. L. Lu et al., "Experimental observation of Weyl points," *Science* **349**, 622 (2015).
27. L. Lu et al., "Symmetry-protected topological photonic crystal in three dimensions," *Nat. Phys.* **12**, 337 (2016).
28. L. Lu, J. D. Joannopoulos, and M. Soljačić, "Topological states in photonic systems," *Nat. Phys.* **12**, 626 (2016).
29. A. B. Khanikaev and G. Shvets, "Two-dimensional topological photonics," *Nat. Photonics* **11**, 763 (2017).
30. H. He et al., "Topological negative refraction of surface acoustic waves in a Weyl phononic crystal," *Nature* **560**, 61 (2018).
31. S. Stutzer et al., "Photonic topological Anderson insulators," *Nature* **560**, 461 (2018).
32. O. Zilberberg et al., "Photonic topological boundary pumping as a probe of 4D quantum Hall physics," *Nature* **553**, 59 (2018).
33. J. Noh et al., "Topological protection of photonic mid-gap defect modes," *Nat. Photonics* **12**, 408 (2018).
34. M. Li et al., "Higher-order topological states in photonic kagome crystals with long-range interactions," *Nat. Photonics* **14**, 89 (2019).
35. Z. Yang et al., "Topological acoustics," *Phys. Rev. Lett.* **114**, 114301 (2015).
36. S. D. Huber, "Topological mechanics," *Nat. Phys.* **12**, 621 (2016).
37. G. Ma, M. Xiao, and C. T. Chan, "Topological phases in acoustic and mechanical systems," *Nat. Rev. Phys.* **1**, 281 (2019).
38. N. P. Armitage, E. J. Mele, and A. Vishwanath, "Weyl and Dirac semimetals in three-dimensional solids," *Rev. Mod. Phys.* **90**, 015001 (2018).
39. T. Ozawa et al., "Topological photonics," *Rev. Mod. Phys.* **91**, 015006 (2019).
40. B. Q. Lv, T. Qian, and H. Ding, "Experimental perspective on three-dimensional topological semimetals," *Rev. Mod. Phys.* **93**, 025002 (2021).
41. C. Simovski, "Spectroscopy, material parameters of metamaterials (a review)," *Opt. Spectrosc.* **107**, 726 (2009).
42. O. Sakai and K. Tachibana, "Technology, plasmas as metamaterials: a review," *Plasma Sources Sci. Technol.* **21**, 013001 (2012).
43. S. Sun et al., "Electromagnetic metasurfaces: physics and applications," *Adv. Opt. Photonics* **11**, 380 (2019).
44. X. Yang et al., "Experimental realization of three-dimensional indefinite cavities at the nanoscale with anomalous scaling laws," *Nat. Photonics* **6**, 450 (2012).
45. A. Poddubny et al., "Hyperbolic metamaterials," *Nat. Photonics* **7**, 948 (2013).
46. Z. Liu et al., "Far-field optical hyperlens magnifying sub-diffraction-limited objects," *Science* **315**, 1686 (2007).
47. P. Shekhar, J. Atkinson, and Z. Jacob, "Hyperbolic metamaterials: fundamentals and applications," *Nano Converg.* **1**, 14 (2014).
48. J. K. Gansel et al., "Gold helix photonic metamaterial as broadband circular polarizer," *Science* **325**, 1513 (2009).
49. S. Zhang et al., "Negative refractive index in chiral metamaterials," *Phys. Rev. Lett.* **102**, 023901 (2009).

50. V. S. Asadchy, A. Díaz-Rubio, and S. Tretyakov, "Bianisotropic metasurfaces: physics and applications," *Nanophotonics* **7**, 1069 (2018).
51. L. Peng et al., "Transverse photon spin of bulk electromagnetic waves in bianisotropic media," *Nat. Photonics* **13**, 878 (2019).
52. S. Sun et al., "Gradient-index meta-surfaces as a bridge linking propagating waves and surface waves," *Nat. Mater.* **11**, 426 (2012).
53. F. Ding, A. Pors, and S. Bozhevolnyi, "Gradient metasurfaces: a review of fundamentals and applications," *Rep. Prog. Phys.* **81**, 026401 (2017).
54. H. Jia et al., "Observation of chiral zero mode in inhomogeneous three-dimensional Weyl metamaterials," *Science* **363**, 148 (2019).
55. L. Zhou and S. T. Chui, "Eigenmodes of metallic ring systems: a rigorous approach," *Phys. Rev. B* **74**, 035419 (2006).
56. R. K. Zhao, T. Koschny, and C. M. Soukoulis, "Chiral metamaterials: retrieval of the effective parameters with and without substrate," *Opt. Express* **18**, 14553 (2010).
57. A. Raman and S. Fan, "Photonic band structure of dispersive metamaterials formulated as a Hermitian eigenvalue problem," *Phys. Rev. Lett.* **104**, 087401 (2010).
58. Y. Liu, G. P. Wang, and S. Zhang, "A nonlocal effective medium description of topological Weyl metamaterials," *Laser Photonics Rev.* **15**, 2100129 (2021).
59. T. Van Mechelen and Z. Jacob, "Photonic Dirac monopoles and skyrmions: spin-1 quantization [Invited]," *Opt. Mater. Express* **9**, 95 (2018).
60. K. Y. Bliokh, D. Smirnova, and F. Nori, "Quantum spin Hall effect of light," *Science* **348**, 1448 (2015).
61. Y. Yang et al., "Topological triply degenerate point with double Fermi arcs," *Nat. Phys.* **15**, 645 (2019).
62. B. Bradlyn et al., "Beyond Dirac and Weyl fermions: unconventional quasiparticles in conventional crystals," *Science* **353**, aaf5037 (2016).
63. W. Gao et al., "Topological photonic phase in chiral hyperbolic metamaterials," *Phys. Rev. Lett.* **114**, 037402 (2015).
64. B. Yang et al., "Direct observation of topological surface-state arcs in photonic metamaterials," *Nat. Commun.* **8**, 97 (2017).
65. M. Xiao, Q. Lin, and S. Fan, "Hyperbolic Weyl point in reciprocal chiral metamaterials," *Phys. Rev. Lett.* **117**, 057401 (2016).
66. C. Zhang et al., "Cycling Fermi arc electrons with Weyl orbits," *Nat. Rev. Phys.* **3**, 660 (2021).
67. B. Yan and C. Felser, "Topological materials: Weyl semimetals," *Annu. Rev. Condens. Matter Phys.* **8**, 337 (2017).
68. B. Q. Lv et al., "Experimental discovery of Weyl semimetal TaAs," *Phys. Rev. X* **5**, 031013 (2015).
69. S. Jia, S. Y. Xu, and M. Z. Hasan, "Weyl semimetals, Fermi arcs and chiral anomalies," *Nat. Mater.* **15**, 1140 (2016).
70. A. A. Soluyanov et al., "Type-II Weyl semimetals," *Nature* **527**, 495 (2015).
71. H. B. Nielsen and M. Ninomiya, "A no-go theorem for regularizing chiral fermions," *Phys. Lett. B* **105**, 219 (1981).
72. H. B. Nielsen and M. Ninomiya, "Absence of neutrinos on a lattice: (I). proof by homotopy theory," *Nucl. Phys. B* **185**, 20 (1981).
73. H. B. Nielsen and M. Ninomiya, "Absence of neutrinos on a lattice: (II). intuitive topological proof," *Nucl. Phys. B* **193**, 173 (1981).
74. D. Friedan, "A proof of the Nielsen-Ninomiya theorem," *Commun. Math. Phys.* **85**, 481 (1982).
75. X. Wan et al., "Topological semimetal and Fermi-arc surface states in the electronic structure of pyrochlore iridates," *Phys. Rev. B* **83**, 205101 (2011).
76. B. Yang et al., "Ideal Weyl points and helicoid surface states in artificial photonic crystal structures," *Science* **359**, 1013 (2018).
77. Ş. K. Özdemir, "Fermi arcs connect topological degeneracies," *Science* **359**, 995 (2018).
78. W. Gao et al., "Photonic Weyl degeneracies in magnetized plasma," *Nat. Commun.* **7**, 12435 (2016).
79. Y. Yang et al., "Ideal unconventional Weyl point in a chiral photonic metamaterial," *Phys. Rev. Lett.* **125**, 143001 (2020).
80. A. A. Soluyanov et al., "Type-II Weyl semimetals," *Nature* **527**, 495 (2015).
81. Z.-M. Yu, Y. Yao, and S. Yang, "Predicted unusual magnetoresponse in type-II Weyl semimetals," *Phys. Rev. Lett.* **117**, 077202 (2016).
82. J. Ma et al., "Nonlinear photoresponse of type-II Weyl semimetals," *Nat. Mater.* **18**, 476 (2019).
83. T. Dubcek et al., "Weyl points in three-dimensional optical lattices: synthetic magnetic monopoles in momentum space," *Phys. Rev. Lett.* **114**, 225301 (2015).
84. M. Xiao et al., "Synthetic gauge flux and Weyl points in acoustic systems," *Nat. Phys.* **11**, 920 (2015).
85. Q. Wang et al., "Optical interface states protected by synthetic Weyl points," *Phys. Rev. X* **7**, 031032 (2017).
86. C. Fang et al., "Topological semimetals with helicoid surface states," *Nat. Phys.* **12**, 936 (2016).
87. A. Zyuzin and A. Burkov, "Topological response in Weyl semimetals and the chiral anomaly," *Phys. Rev. B* **86**, 115133 (2012).
88. D. Son and B. Spivak, "Chiral anomaly and classical negative magnetoresistance of Weyl metals," *Phys. Rev. B* **88**, 104412 (2013).
89. J. Zhou, H.-R. Chang, and D. Xiao, "Plasmon mode as a detection of the chiral anomaly in Weyl semimetals," *Phys. Rev. B* **91**, 035114 (2015).
90. H. Cheng et al., "Vortical reflection and spiraling Fermi arcs with Weyl metamaterials," *Phys. Rev. Lett.* **125**, 093904 (2020).
91. Y. Yang et al., "Veselago lensing with Weyl metamaterials," *Optica* **8**, 249 (2021).
92. H. Jia et al., "Chiral transport of pseudospinors induced by synthetic gravitational field in photonic Weyl metamaterials," *Phys. Rev. B* **104**, 045132 (2021).
93. F. Guinea, M. I. Katsnelson, and A. K. Geim, "Energy gaps and a zero-field quantum Hall effect in graphene by strain engineering," *Nat. Phys.* **6**, 30 (2009).
94. R. Ilan, A. G. Grushin, and D. I. Pikulin, "Pseudo-electromagnetic fields in 3D topological semimetals," *Nat. Rev. Phys.* **2**, 29 (2020).
95. D. Wang et al., "Photonic Weyl points due to broken time-reversal symmetry in magnetized semiconductor," *Nat. Phys.* **15**, 1150 (2019).
96. G.-G. Liu et al., "Observation of Weyl point pair annihilation in a gyromagnetic photonic crystal," arXiv:2106.02461 (2021).
97. Z.-Y. Wang et al., "Realization of an ideal Weyl semimetal band in a quantum gas with 3D spin-orbit coupling," *Science* **372**, 271 (2021).
98. S.-M. Huang et al., "New type of Weyl semimetal with quadratic double Weyl fermions," *Proc. Natl. Acad. Sci. U S A* **113**, 1180 (2016).
99. T. Zhang et al., "Double-Weyl phonons in transition-metal monosilicides," *Phys. Rev. Lett.* **120**, 016401 (2018).
100. H. He et al., "Observation of quadratic Weyl points and double-helicoid arcs," *Nat. Commun.* **11**, 1820 (2020).
101. Q. Yan et al., "Unconventional Weyl exceptional contours in non-Hermitian photonic continua," *Photonics Res.* **9**, 2435 (2021).
102. C. Fang et al., "Topological nodal line semimetals," *Chin. Phys. B* **25**, 117106 (2016).
103. Q. Xu et al., "Topological nodal line semimetals in the CaP_3 family of materials," *Phys. Rev. B* **95**, 045136 (2017).
104. J.-M. Carter et al., "Semimetal and topological insulator in perovskite iridates," *Phys. Rev. B* **85**, 115105 (2012).
105. G. van Miert, C. Ortix, and C. M. Smith, "Topological origin of edge states in two-dimensional inversion-symmetric insulators and semimetals," *2D Mater.* **4**, 015023 (2016).
106. G. Bian et al., "Drumhead surface states and topological nodal-line fermions in $TlTaSe_2$," *Phys. Rev. B* **93**, 121113 (2016).

107. Y.-H. Chan et al., "Ca_3P_2 and other topological semimetals with line nodes and drumhead surface states," *Phys. Rev. B* **93**, 205132 (2016).
108. W. Gao et al., "Experimental observation of photonic nodal line degeneracies in metacrystals," *Nat. Commun.* **9**, 950 (2018).
109. L. Xia et al., "Observation of hourglass nodal lines in photonics," *Phys. Rev. Lett.* **122**, 103903 (2019).
110. E. Yang et al., "Observation of non-Abelian nodal links in photonics," *Phys. Rev. Lett.* **125**, 033901 (2020).
111. Q. Guo et al., "Experimental observation of non-Abelian topological charges and edge states," *Nature* **594**, 195 (2021).
112. A. Demetriadou and J. B. Pendry, "Taming spatial dispersion in wire metamaterial," *J. Phys. Condens. Matter* **20**, 295222 (2008).
113. B. Zheng et al., "Hourglass phonons jointly protected by symmorphic and nonsymmorphic symmetries," *Phys. Rev. B* **104**, L060301 (2021).
114. Q. Wu, A. A. Soluyanov, and T. Bzdusek, "Non-Abelian band topology in noninteracting metals," *Science* **365**, 1273 (2019).
115. T. Jiang et al., "Four-band non-Abelian topological insulator and its experimental realization," *Nat. Commun.* **12**, 6471 (2021).
116. S. M. Young et al., "Dirac semimetal in three dimensions," *Phys. Rev. Lett.* **108**, 140405 (2012).
117. Z. Liu et al., "Discovery of a three-dimensional topological Dirac semimetal, Na_3Bi," *Science* **343**, 864 (2014).
118. S. Borisenko et al., "Experimental realization of a three-dimensional Dirac semimetal," *Phys. Rev. Lett.* **113**, 027603 (2014).
119. Q. Guo et al., "Three dimensional photonic Dirac points in metamaterials," *Phys. Rev. Lett.* **119**, 213901 (2017).
120. Q. Guo et al., "Observation of three-dimensional photonic Dirac points and spin-polarized surface arcs," *Phys. Rev. Lett.* **122**, 203903 (2019).
121. S. Ma et al., "Linked Weyl surfaces and Weyl arcs in photonic metamaterials," *Science* **373**, 572 (2021).
122. A. B. Khanikaev et al., "Photonic topological insulators," *Nat. Mater.* **12**, 233 (2013).
123. K. Hasebe, "SO(5) Landau models and nested Nambu matrix geometry," *Nucl. Phys. B* **956**, 115012 (2020).
124. C. N. Yang, "SU2 monopole harmonics," *J. Math. Phys.* **19**, 2622 (1978).
125. C. N. Yang, "Generalization of Dirac's monopole to SU2 gauge fields," *J. Math. Phys.* **19**, 320 (1978).
126. B. Lian and S. C. Zhang, "Five-dimensional generalization of the topological Weyl semimetal," *Phys. Rev. B* **94**, 041105 (2016).
127. B. Lian and S. C. Zhang, "Weyl semimetal and topological phase transition in five dimensions," *Phys. Rev. B* **95**, 235106 (2017).
128. J. Y. Chen, B. Lian, and S. C. Zhang, "Doubling theorem and boundary states of five-dimensional Weyl semimetal," *Phys. Rev. B* **100**, 075112 (2019).
129. X. L. Qi, T. L. Hughes, and S. C. Zhang, "Topological field theory of time-reversal invariant insulators," *Phys. Rev. B* **78**, 195424 (2008).
130. Y. Yang et al., "Realization of a three-dimensional photonic topological insulator," *Nature* **565**, 622 (2019).
131. B. Yang et al., "Momentum space toroidal moment in a photonic metamaterial," *Nat. Commun.* **12**, 1784 (2021).
132. R. S. Mong, J. H. Bardarson, and J. E. Moore, "Quantum transport and two-parameter scaling at the surface of a weak topological insulator," *Phys. Rev. Lett.* **108**, 076804 (2012).
133. T. Kaelberer et al., "Toroidal dipolar response in a metamaterial," *Science* **330**, 1510 (2010).
134. N. Papasimakis et al., "Electromagnetic toroidal excitations in matter and free space," *Nat. Mater.* **15**, 263 (2016).
135. N. A. Spaldin, M. Fiebig, and M. Mostovoy, "The toroidal moment in condensed-matter physics and its relation to the magnetoelectric effect," *J. Phys. Condens. Matter.* **20**, 434203 (2008).
136. D. Xiao, W. Yao, and Q. Niu, "Valley-contrasting physics in graphene: magnetic moment and topological transport," *Phys. Rev. Lett.* **99**, 236809 (2007).
137. S. Roy et al., "Tunable axial gauge fields in engineered Weyl semimetals: semiclassical analysis and optical lattice implementations," *2D Mater.* **5**, 024001 (2018).
138. T. Dubček et al., "Weyl points in three-dimensional optical lattices: synthetic magnetic monopoles in momentum space," *Phys. Rev. Lett.* **114**, 225301 (2015).
139. J. Bravo-Abad et al., "Weyl points in photonic-crystal superlattices," *2D Mater.* **2**, 034013 (2015).
140. Q. Wang et al., "Optical interface states protected by synthetic Weyl points," *Phys. Rev. X* **7**, 031032 (2017).
141. T. Ochiai, "Floquet–Weyl and Floquet-topological-insulator phases in a stacked two-dimensional ring-network lattice," *J. Phys. Condens. Matter* **28**, 425501 (2016).
142. H. Wang, L. Zhou, and Y. D. Chong, "Floquet Weyl phases in a three-dimensional network model," *Phys. Rev. B* **93**, 144114 (2016).
143. Y. Lu et al., "Probing the Berry curvature and Fermi arcs of a Weyl circuit," *Phys. Rev. B* **99**, 020302 (2019).
144. K. Luo, R. Yu, and H. Weng, "Topological nodal states in circuit lattice," *Research* **2018**, 6793752 (2018).
145. F. Mei et al., "Witnessing topological Weyl semimetal phase in a minimal circuit-QED lattice," *Quantum Sci. Technol.* **1**, 015006 (2016).
146. Z. Xiong et al., "Hidden-symmetry-enforced nexus points of nodal lines in layer-stacked dielectric photonic crystals," *Light Sci. Appl.* **9**, 176 (2020).
147. T. Kawakami and X. Hu, "Symmetry-guaranteed nodal-line semimetals in an FCC lattice," *Phys. Rev. B* **96**, 235307 (2017).
148. Q. Yan et al., "Experimental discovery of nodal chains," *Nat. Phys.* **14**, 461 (2018).
149. W. Deng et al., "Nodal rings and drumhead surface states in phononic crystals," *Nat. Commun.* **10**, 1769 (2019).
150. H. Wang et al., "Three-dimensional photonic Dirac points stabilized by point group symmetry," *Phys. Rev. B* **93**, 235155 (2016).
151. A. Slobozhanyuk et al., "Three-dimensional all-dielectric photonic topological insulator," *Nat. Photonics* **11**, 130 (2017).
152. H.-X. Wang et al., "Type-II Dirac photons," *NPJ Quantum Mater.* **2**, 54 (2017).
153. A. B. Khanikaev et al., "Photonic topological insulators," *Nat. Mater.* **12**, 233 (2013).
154. X. Cheng et al., "Robust reconfigurable electromagnetic pathways within a photonic topological insulator," *Nat. Mater.* **15**, 542 (2016).
155. T. Ma and G. Shvets, "All-Si valley-Hall photonic topological insulator," *New J. Phys.* **18**, 025012 (2016).
156. C. He et al., "Photonic topological insulator with broken time-reversal symmetry," *Proc. Natl. Acad. Sci. U S A* **113**, 4924 (2016).
157. A. B. Khanikaev et al., "Photonic topological insulators," *Nat. Mater.* **12**, 233 (2013).
158. N. Shahrubudin, T. C. Lee, and R. Ramlan, "An overview on 3D printing technology: technological, materials, and applications," *Procedia Manuf.* **35**, 1286 (2019).
159. C. Liu et al., "Disorder-induced topological state transition in photonic metamaterials," *Phys. Rev. Lett.* **119**, 183901 (2017).
160. C. Liu et al., "Disorder-immune photonics based on Mie-resonant dielectric metamaterials," *Phys. Rev. Lett.* **123**, 163901 (2019).
161. X. N. Liu et al., "An elastic metamaterial with simultaneously negative mass density and bulk modulus," *Appl. Phys. Lett.* **98**, 251907 (2011).

162. X. Zhou, X. Liu, and G. Hu, "Elastic metamaterials with local resonances: an overview," *Theor. Appl. Mech. Lett.* **2**, 041001 (2012).
163. L. Lu, H. Gao, and Z. Wang, "Topological one-way fiber of second Chern number," *Nat. Commun.* **9**, 1 (2018).
164. L. Wang, S.-K. Jian, and H. Yao, "Topological photonic crystal with equifrequency Weyl points," *Phys. Rev. A* **93**, 061801 (2016).
165. J. Xiong et al., "Evidence for the chiral anomaly in the Dirac semimetal Na_3Bi," *Science* **350**, 413 (2015).
166. L. Zhang, X.-Y. Song, and F. Wang, "Quantum oscillation in narrow-gap topological insulators," *Phys. Rev. Lett.* **116**, 046404 (2016).
167. P. L. Cai et al., "Drastic pressure effect on the extremely large magnetoresistance in WTe_2: quantum oscillation study," *Phys. Rev. Lett.* **115**, 057202 (2015).
168. G. Rosenberg, H.-M. Guo, and M. Franz, "Wormhole effect in a strong topological insulator," *Phys. Rev. B* **82**, 041104 (2010).
169. Y. Yang et al., "Synthesis and observation of non-Abelian gauge fields in real space," *Science* **365**, 1021 (2019).
170. Y. Yang et al., "Non-Abelian generalizations of the Hofstadter model: spin-orbit-coupled butterfly pairs," *Light Sci. Appl.* **9**, 177 (2020).
171. R. El-Ganainy et al., "Non-Hermitian physics and PT symmetry," *Nat. Phys.* **14**, 11 (2018).
172. C. M. Bender, "Making sense of non-Hermitian Hamiltonians," *Rep. Prog. Phys.* **70**, 947 (2007).
173. S. Yu, X. Piao, and N. Park, "Topological hyperbolic lattices," *Phys. Rev. Lett.* **125**, 053901 (2020).
174. E. Lustig, Y. Sharabi, and M. Segev, "Topological aspects of photonic time crystals," *Optica* **5**, 1390 (2018).
175. G. G. Liu et al., "Topological Anderson insulator in disordered photonic crystals," *Phys. Rev. Lett.* **125**, 133603 (2020).
176. W. A. Benalcazar, B. A. Bernevig, and T. L. Hughes, "Quantized electric multipole insulators," *Science* **357**, 61 (2017).
177. S. Liu et al., "Octupole corner state in a three-dimensional topological circuit," *Light Sci. Appl.* **9**, 145 (2020).
178. B. Xie et al., "Higher-order band topology," *Nat. Rev. Phys.* **3**, 520 (2021).